Juan de Fuca subduction zone from a mixture of tomography and waveform modeling

Risheng Chu,[1] Brandon Schmandt,[1] and Don V. Helmberger[1]

Received 10 January 2012; accepted 13 January 2012; published 9 March 2012.

[1] Seismic tomography images of the upper mantle structures beneath the Pacific Northwestern United States display a maze of high-velocity anomalies, many of which produce distorted waveforms evident in the USArray observations indicative of the Juan de Fuca (JdF) slab. The inferred location of the slab agrees quite well with existing contour lines defining the slab's upper interface. Synthetic waveforms generated from a recent tomography image fit teleseismic travel times quite well and also some of the waveform distortions. Regional earthquake data, however, require substantial changes to the tomographic velocities. By modeling regional waveforms of the 2008 Nevada earthquake, we find that the uppermost mantle of the 1D reference model AK135, the reference velocity model used for most tomographic studies, is too fast for the western United States. Here, we replace AK135 with mT7, a modification of an older Basin-and-Range model T7. We present two hybrid velocity structures satisfying the waveform data based on modified tomographic images and conventional slab wisdom. We derive *P* and *SH* velocity structures down to 660 km along two cross sections through the JdF slab. Our results indicate that the JdF slab is subducted to a depth of 250 km beneath the Seattle region, and terminates at a shallower depth beneath Portland region of Oregon to the south. The slab is about 60 km thick and has a *P* velocity increase of 5% with respect to mT7. In order to fit waveform complexities of teleseismic Gulf of Mexico and South American events, a slab-like high-velocity anomaly with velocity increases of 3% for *P* and 7% for *SH* is inferred just above the 660 discontinuity beneath Nevada.

Citation: Chu, R., B. Schmandt, and D. V. Helmberger (2012), Juan de Fuca subduction zone from a mixture of tomography and waveform modeling, *J. Geophys. Res.*, *117*, B03304, doi:10.1029/2012JB009146.

1. Introduction

[2] USArray data analysis has produced abundant seismic images for the upper mantle velocity structures beneath the western United States using surface-wave dispersion data [*Nettles and Dziewoński*, 2008; *Pollitz and Snoke*, 2010; *Moschetti et al.*, 2010], travel times of teleseismic body waves [*Sigloch et al.*, 2008, *Burdick et al.*, 2008, *Schmandt and Humphreys*, 2010; *Xue and Allen*, 2010], and joint inversions [*Tian et al.*, 2011; *Obrebski et al.*, 2011]. Since knowledge of velocity perturbations in the crust and upper mantle is key to the understanding of mantle dynamics and its surface manifestations, higher-resolution images are always preferred [*Boschi et al.*, 2010].

[3] Among the various inversion techniques, travel-time tomography using arrival times of teleseismic earthquakes is a common approach [*Gao et al.*, 2004]. However, any type of seismic inversion usually involves damping and smoothing, which greatly reduces the sharpness of the final images. Tomography inversions are especially difficult for subduction zones, such as Cascadia, that lack deep slab seismicity. This may be the reason that coastal models derived from the USArray data set do not closely resemble morphologies of the downgoing plates created by dynamic models [e.g., *Burkett and Billen*, 2010].

[4] Seismic tomography using waveform data has made significant advances in recent years with the development of the "adjoint methodology" [*Tape et al.*, 2007]. Nonetheless, the identification and modeling of event-station paths that are the most sensitive to the velocity perturbations can serve two important purposes. The first is to produce possible models that fit key data (which may be sparse) and, second, to establish data sets as well as starting models for future adjoint inversions. *Song and Helmberger* [2007a, 2007b] implemented an analogous approach where they took an intermediate step to validate tomographic velocities by comparing synthetic seismograms against observed waveforms. The basic idea is displayed in Figure 1a. The high-velocity slab that dips to the southeast has a strong impact on the wavefield and makes the waveform complexity azimuthally dependent. The *P* and *SH* waveforms recorded by the La Ristra array display such a pattern where events from the southeast (SE) have lower amplitudes and longer durations than events from the northwest (NW). *Sun and Helmberger* [2011] exploited the pattern of waveform

[1]Seismological Laboratory, California Institute of Technology, Pasadena, California, USA.

0148-0227/12/2012JB009146

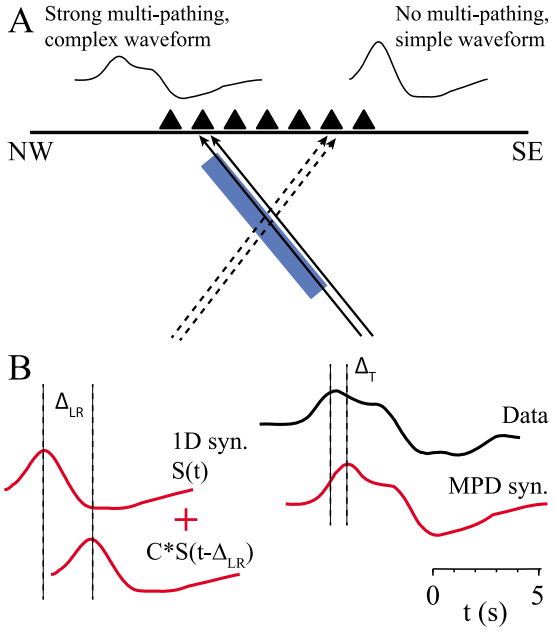

Figure 1. (a) An illustration of azimuthal variations of waveform complexity for a SE-dipping high-velocity slab. For raypaths arriving from the SE, multiple seismic signals can be recorded at the same station. An earlier signal travels through the high-velocity slab, while a later signal travels along the slower outside edge. The separation of these two signals is Δ_{LR}. Travel time residual with respect to a reference model is denoted as Δ_T. For waves arriving from the NW, Δ_{LR} will be small because the differential path lengths across the slab are negligible in this direction. Thus, no multipathing will be observed [*Sun*, 2009]. (b) An illustration of how the multipathing detector (MPD) works (see the main text for details). Comparison of example data (black) and MPD synthetics (red) is shown on the right.

distortions to detect dipping structures and map out complexities in the wavefields.

[5] Although there are more advanced parameterizations to describe the observed waveform complexities, a simple two-pulse waveshape modeling captures the most significant features [*Sun and Helmberger*, 2011]. Whereas conventional tomography assumes uniform pulse shapes, this new method provides a measure of splitting time between these two pulses (Figure 1b). Starting with synthetics from a 1D reference model such as AK135, we search for the time difference Δ_{LR} and amplitude ratio C between the two pulses to fit the observed waveform complexity [*Sun and Helmberger*, 2011]. The travel-time residual Δ_T is obtained by cross correlating the synthetic waveform with the observation. Note that signals from the SE arrive early so that travel-time residuals, observed arrival time minus theoretical arrival time, will be negative. Since fast travel-time residuals correlate with multipathing, the product of $(\Delta_T \times \Delta_{LR})$ becomes negative, indicating dipping fast structures (DFS). The other functional that highlights sharp edges is the product of the sharpest changes in travel times, or the gradient of the first arrival residuals $\nabla(\Delta_T)$, with time difference Δ_{LR}.

[6] *Sun and Helmberger* [2011] applied this method to *SH*-waveform data sampling our study region from various azimuths. Data from the SE display the strongest waveform complexities associated with the JdF slab, which is the most prominent DFS feature observed along the Pacific coast (Figures 2a and 2b). The location of the JdF slab from the mapping of *SH*-waveform complexities agrees quite well with the tomographic imaging (Figure 2c), even the weak zones south of the Washington-Oregon border where the JdF slab is not obvious (Figures 2a and 2c). Two sharp edges occur near the eastern end of the Cape Mendocino transform fault and near Seattle where the JdF slab changes its strike to the NW (Figure 3). *Sun and Helmberger* [2011] find that the *SH*-waveform splitting (Δ_{LR}) along the slab varies from 4.0 to 6.0 s which suggests an *S* velocity change of 6.5% over 250 km. We display a recent *P* wave tomographic image by *Schmandt and Humphreys* [2010], noted as SCH, showing a clear N-S high-velocity strip running down to the Mendocino transform fault (MTF) in the Pacific northwest and various features associated with the Snake-River Plains (SRP) (Figure 2c). Their image of the JdF slab extends to a depth of about 300 km with a *P* velocity increase of about 2.5% beneath Seattle area (Figure 2d), which is comparable to the values given by waveform complexity [*Sun and Helmberger*, 2011]. There is also another abrupt change at about 46.5°N where the mapped edges of the JdF changes its strike to about N40°E. This edge is produced by the deeper high-velocity anomaly located beneath Nevada and is roughly 2D in nature [*Sun and Helmberger*, 2011]. A preview of our hybrid velocity structure constructed from forward modeling the waveform data and travel times along the same profile is shown in Figure 2e.

[7] Beneath Japan, some tomographic images of the seismic structure have added constraints on the slab shape that resembles morphologies of a downgoing plate [*Zhao et al.*, 1994]. They fix the slab's top to the plate interface, which is inferred from seismicity. We will follow such an approach here except that we will model the complex waveforms recorded along the narrow corridors including the Seattle area (R1) and including the Portland area (R2) (Figure 3). These two corridors are sampled by various seismic profiles that are assumed to be roughly 2D.

[8] Modeling seismograms in the western United States has a long history starting from the Vela-Uniform project developed in the 1960s to monitor explosions. Linear arrays of seismic stations, Long Range Seismic Measurements (LRSM) that resemble more recent linear PASSCAL deployments, were set out to record large explosions. One of the first demonstrations of upper mantle lateral variations was published by *Romney et al.* [1962] and showed east to west variations of travel times and amplitudes for the Gnome explosion fired in New Mexico. They found that the recorded P_n amplitudes to the west dropped off suddenly by a factor of 10 at a distance of about 1000 km. Another reversed profile from the large BOXCAR explosion at Nevada Test Site displayed a shadow-zone feature at about 900 km. The observations of both the accurate travel times and amplitude-decay behaviors were used to develop a low-velocity-zone structure in model T7 shown in Figure 4 [*Helmberger*, 1973; *Burdick and Helmberger*, 1978]. A longer reversed profile from a west Texas earthquake recorded by networks along the west coast largely was used

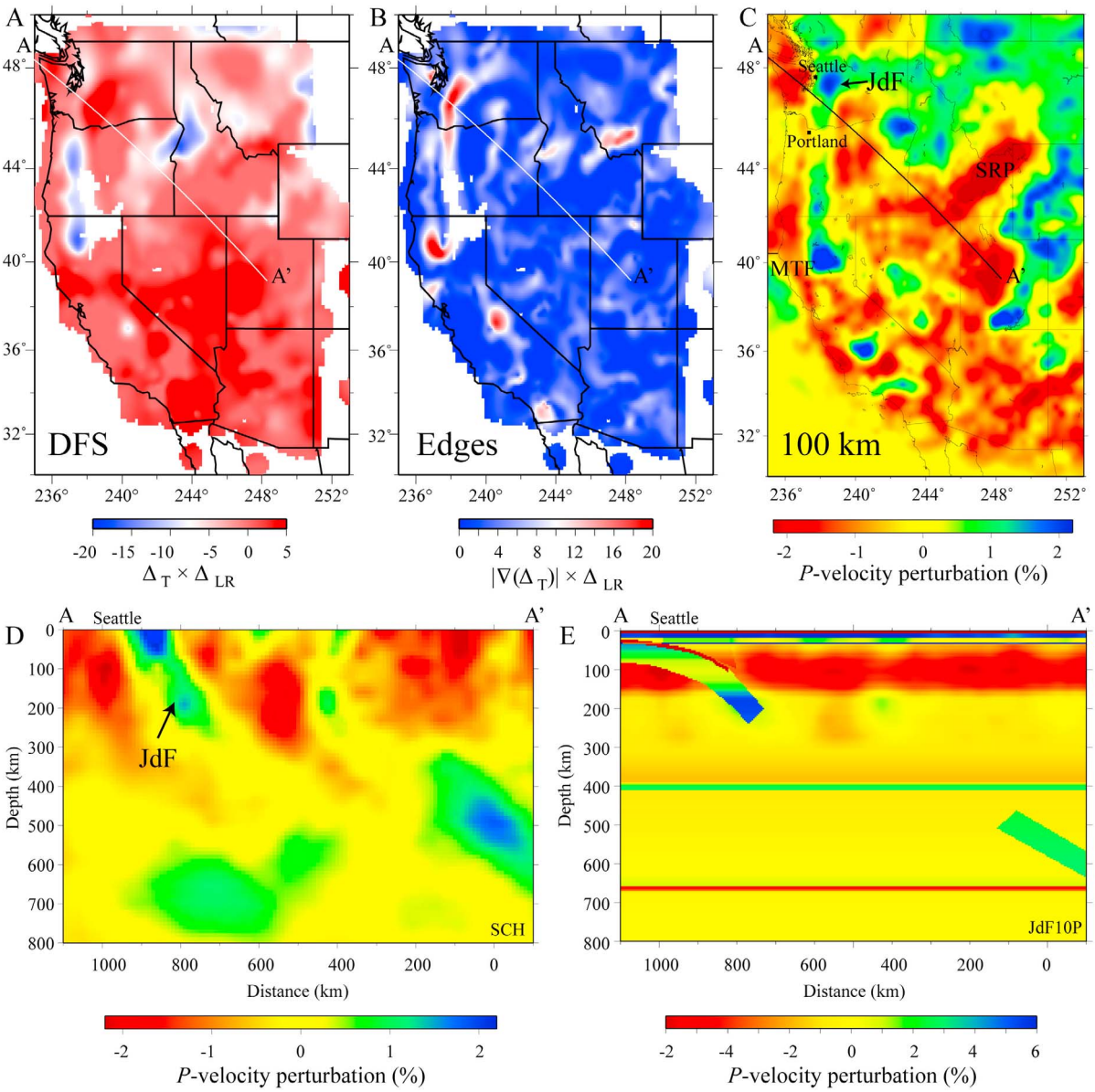

Figure 2. Seismic structures derived from observed waveform complexities showing (a) dipping fast structure (DFS) and (b) the edges of the Juan de Fuca slab (JdF) [*Sun and Helmberger*, 2011]. (c) Map view of a tomographic image at 100 km for the western United States (from *Schmandt and Humphreys* [2010, hereinafter referred to as SCH]). The location of JdF slab derived from waveform complexity agrees with the slab from travel-time tomography. (d) We show tomographic *P* wave velocities of the Juan de Fuca (JdF) slab from *Schmandt and Humphreys* [2010], and (e) the hybrid model constructed from forward modeling of waveform data and travel times. The location of the cross section is shown as AA′ in the map. Note the difference between the color scales in Figures 2 d and 2e. In Figure 2c, MTF refers to the Cape Mendocino transform fault and SRP is the Snake River plain.

to validate this simple 1D structure for western U.S. [*Melbourne and Helmberger*, 1998]. However, along our corridors, the uppermost mantle does not require a thin lid between 35 and 70 km, and a modified 1D structure was derived named mT7 (Figure 4).

[9] The objective of this study is to modify the SCH tomographic structures observed by *Schmandt and Humphreys* [2010] by first changing the 1D reference model to mT7 and then incorporating the slab structures displayed in Figure 3 to better explain the observed waveform complexity. To achieve this goal, we divide this study into five sections. The first section describes the earthquake data and the routine processing used in this study. We then address the construction of synthetics and replacing the reference models as given in the Appendix A for readers not accustomed to waveform modeling. In the next section, we address the modeling of the regional seismic profile, followed by the *P* and *SH* waveform modeling as discussed in

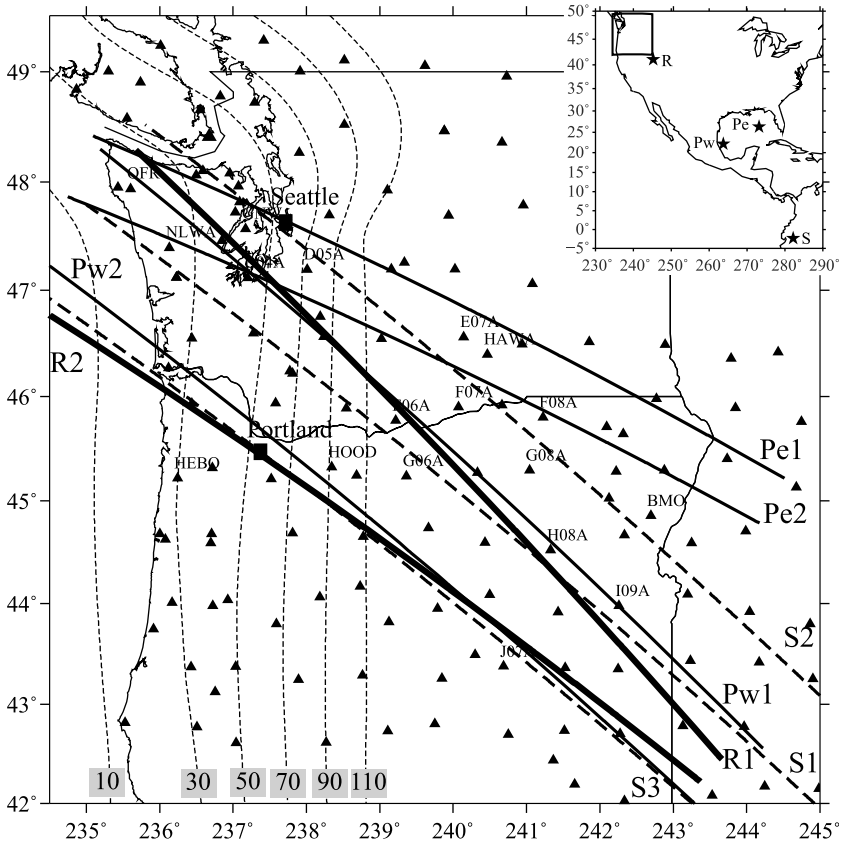

Figure 3. Map of the Pacific Northwest showing USArray stations, and corridors of our modeling efforts. Black triangles denote broadband seismic stations deployed in this area. Dashed lines represent the top of the subducting Juan de Fuca slab with depth changing from 10 km to 110 km with depths labeled [*McCrory et al.*, 2006]. Thick solid lines R1 and R2 are regional *P* profiles from the 2008 Nevada event. Thin solid lines are four *P* profiles from the 2006 and 2007 Gulf of Mexico earthquakes (Pe1, Pe2, Pw1, and Pw2). Thick dashed lines display three *SH* profiles from a 2007 South American earthquake (S1, S2, and S3). Locations of the earthquakes are shown in the inset with a box indicating our study area. The upper JdF slab structure is investigated along two corridors, R1 and R2, which are inferred to have different lengths of slabs. Pw2 and S3 are profiles of *P* and *S* waveforms used in validating the R2 structure while the other sections sample the R1 corridor in more detail (R1 and R2 are discussed in sections 2–4).

section 4. Section 5 addresses the corridor R2, followed by a discussion in section 6. All of the waveform data are modeled by 2D velocity structures containing two imposed slab structures, one shallow and one deep as shown in Figure 2e.

2. Earthquake Data

[10] Because the JdF slab is dipping to the east (Figure 2), arrivals from this direction provide the most defining observations as discussed earlier. However, it is difficult to find events arriving from the east with good distance coverage and simple source time functions mainly because of the stable North America plate to the east. After examined record sections from various events, we chose four earthquakes that provide the best observations of both regional and teleseismic paths (Figure 2 and Table 1). The nearest earthquake occurred in Northern Nevada. Two events are in the Gulf of Mexico (Pe and Pw), and even though they are shallow earthquakes they show depth phases. A deep event from South America is selected where both the direct arrival and the depth phases can be used. Waveform data for these four earthquakes is obtained through the IRIS Data Management Center. We remove instrument responses and resample the data to a rate of 10 samples per second. The vertical displacements are band-pass filtered at a frequency range of 0.02 Hz to 1.0 Hz.

[11] Mechanisms for the teleseismic earthquakes are global CMT solutions. The regional event in Northern Nevada has a well-known mechanism, depth, and source parameters [*Wei et al.*, 2009]. Accurate source parameters, including location and origin time, are particularly important to remove uncertainties in base-line shifts normally involved in assuming reference models by teleseismic body wave tomography. Therefore, synthetic and observed waveforms for the regional earthquake are aligned on the absolute travel times with no base-line shifts allowed. Small time shifts are allowed for teleseismic earthquakes, as applied in teleseismic tomography.

3. Waveform Modeling Along Corridor R1

[12] First, we concentrate on the regional profile, Corridor R1 from the Nevada earthquake, which is the closest to 2D in nature (Figure 3). To validate the tomography velocities

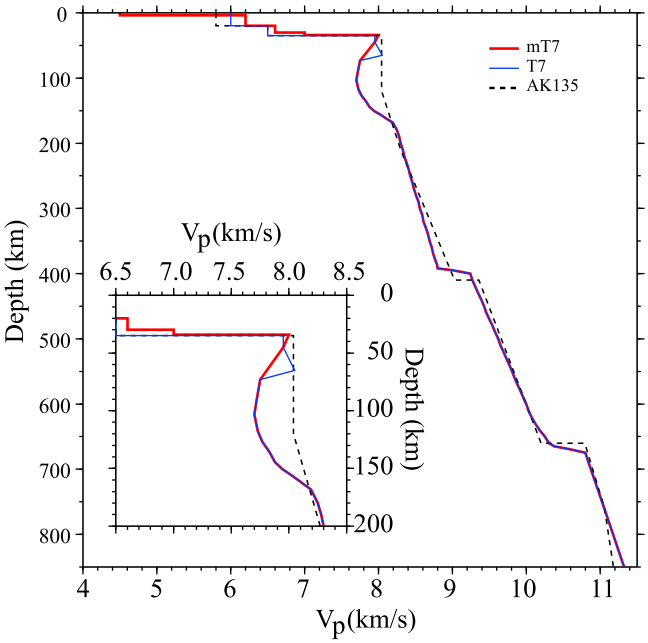

Figure 4. Comparison of 1D *P* velocity models of AK135 (black), mT7 (red), and T7 (blue). Model mT7 is derived from T7 by removing the lid structure between 35 and 70 km in the uppermost mantle. The top 200 km of the models are enlarged in the inset. The *P* velocity is about 7.7 km/s in the LVZ for T7 and mT7, which is a 5% reduction relative to the model AK135.

and test the 1D model mT7, we calculate synthetic seismograms for the Nevada earthquake (Table 1) at regional distances using the *Schmandt and Humphreys'* [2010] tomographic structure labeled SCH-AK and the 1D model mT7 (Figure 5). Synthetics produced by the tomographic velocities are about 1.0 to 6.0 s faster than data as the distances increase, which is primarily caused by the relatively fast 1D reference AK135 (Figure 4). Synthetics produced by mT7 work much better in explaining the P_n arrival times and waveforms by producing the observed broadening of the P_n wave between 500 and 900 km. The 1D model mT7 can also predict the transition from P_n wave to *P* wave at the distances of 800–900 km (Figure 5b). The rapid change in the data between D05A and D04A is observed along a zone directly above the tomographic JdF slab (Figure 2c) and correlates with the NS multipathing edge (Figure 2b), which suggests that 2D structures are still required such as adding the slab-like perturbations to the mT7 model.

[13] We change the 1D reference of *Schmandt and Humphreys* [2010] to mT7. This hybrid tomographic structure is labeled SCH-mT7. The comparison of data and synthetic waveforms from this new model is shown in Figure 6a. Changing the reference model in the upper 200 km has little effect on the steeply incident teleseismic raypaths used in the tomography inversion, but is critical for fitting rays that turn within the uppermost mantle. Lateral changes in teleseismic ray position are all < 15 km and model node spacing is 40 km beneath USArray. In Figure 6a we add timing lines for P_n versus *P* to emphasize the changeover associated with the shadow zone produced by the low-velocity layer of mT7. The synthetic *P* waveforms are about 1.0–2.0 s late between 950 and 1100 km, which indicates that the velocity perturbation of the tomographic slab is not fast enough. A new hybrid structure JdF10 with a higher-velocity perturbation for the JdF slab (5%) solves this problem. It reduces the variance of travel-time residuals from 1.15 s to 0.33 s (Figure 6b). WKM raypaths (see Appendix A) are shown to indicate the impact of adding the faster slab to the tomographic structures.

[14] JdF10 consists of tomographic velocity perturbations above 300 km from SCH. Below 300 km, it is basically the 1D model mT7. The slab is constructed using the upper interface of the JdF slab [from *McCrory et al.*, 2006] assuming a constant velocity perturbation. A 10 km low-velocity layer from *Nikulin et al.* [2009] for station GNW is embedded on top of the slab to represent the subducting oceanic crust (7 km/s). The slab structure is determined by fitting both regional and teleseismic data through a grid search using different velocity perturbations for the mantle portion of the slab (3%, 5%, and 7% of the slab), slab thicknesses (60 km, 70 km, and 80 km), and slab depths (200 km, 250 km, and 300 km). The best results are a 60 km thick slab with *P* velocity increase of 5% subducting to a depth of 250 km. We have also added the low velocity beneath the slab to match the previously modeled Pacific margin structures [*Melbourne and Helmberger*, 2001].

[15] Figure 7 shows a blow up of the observed *P* wave record section at larger distances along with timing lines indicating predictions from three models, SCH-AK, SCH-mT7, and JdF10. We have extended the data to the north by including Canadian stations. Synthetics produced by JdF10 fit the observed travel time quite well. At some stations, denoted by dashed traces (Figure 7d), the recorded waves appear to be slightly early, which may be caused by a faster slab and/or less slow-zone beneath these westernmost stations. In short, we have made some adjustments to the tomographic velocity model SCH to explain these regional observations. Next, we return to the teleseismic data and retest the new hybrid structure against the more distant *P* and *S* waveform data.

4. Testing and Refining Regional Models

[16] In the velocity structure JdF10, we only include the velocity perturbations above 300 km from the tomographic model SCH. To test the importance of deep anomalies, we add velocity perturbations of SCH below 300 km to JdF10, denoted as JdF10+. We start with the *P* wave profile Pw1 from the earthquake in the western Gulf of Mexico and compare it with synthetic predictions from these two velocity structures (Figure 8). We find that the data fits JdF10 as well as the original SCH at distances greater than 3100 km.

Table 1. Earthquake Locations and Mechanisms Used in This Study

ID	Date	Latitude	Longitude	Depth (km)	M_w	Strike	Dip	Rake
R	2008/02/21	41.08	245.23	10.0	6.3	203	47	−99
Pw	2007/05/23	22.16	263.72	10.0	5.6	124	52	61
Pe	2006/09/10	26.32	273.16	29.6	5.9	192	89	−170
S	2007/11/16	−2.31	282.16	122.90	6.7	177	29	−44

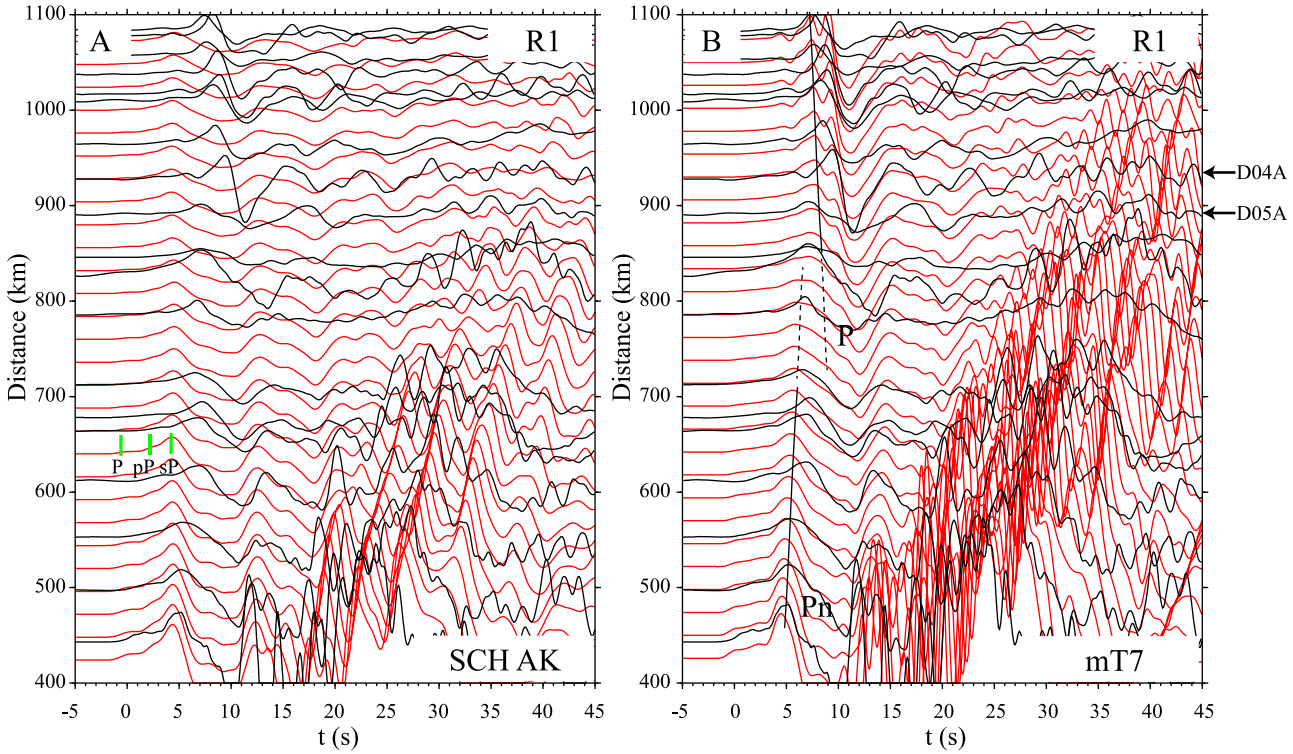

Figure 5. Comparison of finite difference (FD) synthetics (red) and vertical displacements (black) observed along the line R1 from the Nevada earthquake for (a) tomographic model SCH with AK135 as background [*Schmandt and Humphreys*, 2010] and (b) 1D velocity model mT7 [*Burdick and Helmberger*, 1978]. Displacement data of all earthquakes is band-pass filtered using corner frequencies at 0.02 Hz and 1.0 Hz after removing instrument responses. Synthetics from the tomographic velocity model (SCH-AK) arrive 1.0–6.0 s earlier than observed data, which suggests that the uppermost mantle of AK135 is not appropriate for the Pacific Northwest. The synthetics contain the contributions of *P* (small) and two depth phases *pP* and *sP* (large) as indicated by the green bars. The phase *sP* is the strongest pulse assuming the thrust mechanism obtained by *Wei et al.* [2009]. Synthetics from the 1D model mT7 produce better fits to the waveforms and travel times, where the transition from P_n to *P* occurs at about 800–900 km. P_n and *P* are denoted by black lines with dashed lines marking the transition.

However, because we changed the 1D reference, the synthetics at shorter distances become progressively late as expected from the modeling presented in Appendix A. Some stations become particularly late because of the deep slow structure in SCH (i.e., N14A, Figure 8). On the right, synthetics produced by JdF10 fit the data quite well. The observed waveforms at stations F06A and F07A appear to be multipathed apparently caused by a sharp edge where Δ_T varies rapidly. Their amplitudes are lower when plotted in true scale (Figure 9). Waveforms at neighboring stations are likewise complicated and weak, indicative of multipathing. For *S* waveforms from the South American event (Table 1), the similar phenomenon is observed [*Sun and Helmberger*, 2011]. The *SH* data has smaller incident angles which corresponds to the different locations of the multipathed waveforms (Figure 9). *Sun and Helmberger* [2011] modeled the multipathed waveforms by inserting a fast slab in the transition zone, referred to as the Farallon slab [*Sigloch et al.*, 2008]. There is some debate about what this structure is and where it comes from. We will label it the Deep Nevada Transition Structure (DNTS) to avoid a direct interpretation at this stage. This feature appears in the transition zone in the southeastern half of the S1 and S2 cross sections (Figure 3).

[17] We insert a deeper high-velocity anomaly into JdF10 to explain the observed multipathing (Figure 10). The new structure is referred to as JdF10P. Since we rely on a grid-search approach, we follow a procedure similar to that used by *Chen et al.* [2007] to construct a simple slab with relatively sharp edges, which are expected from thermal modeling [e.g., *van Keken et al.*, 2002] but penalized by regularization in tomography models. We allow the anomaly to flatten above the 660 discontinuity (Figure 10), but with one segment dipping upward roughly along the plane of the *P* wave raypaths. We then adjust the geometry and velocity increases of the anomaly to match both travel time and amplitude for event S, as in the work of *Sun and Helmberger* [2011]. Note that the waveforms become broadened starting from station G08A; station F06A displays two pulses caused by the sharp bottom edge of the deep anomaly. The waveform fits are improved over those in Figure 8 but there are likely 3D features as well (see *Sun and Helmberger* [2011, Figure 6] for such complexities). The travel times fit quite well with travel-time residuals reduced from 0.17 s to 0.04 s.

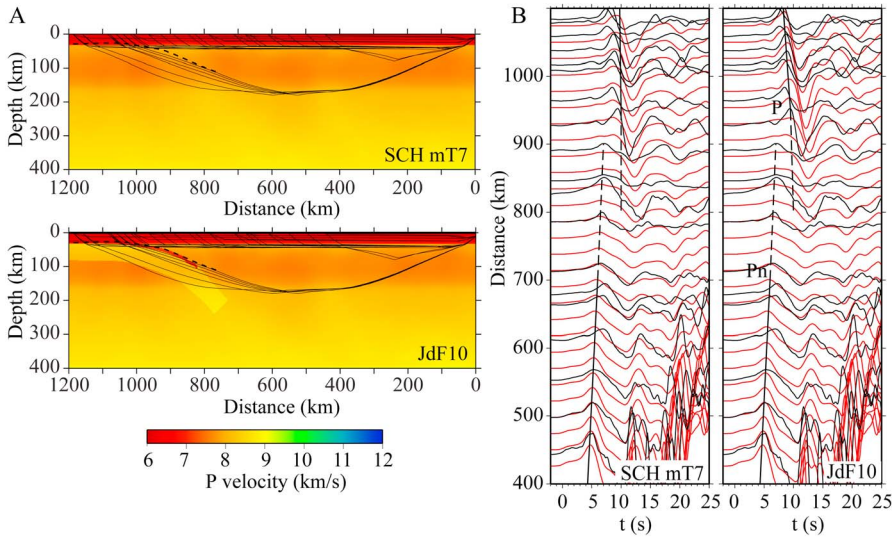

Figure 6. (a) The *P* velocity models of SCH with mT7 as (top) background and (bottom) JdF10 for regional profile R1 of the Nevada earthquake. (b) Comparison of FD synthetics (red) and observed vertical displacements (black) for (left) SCH-mT7 and (right) JdF10. In model JdF10, the JdF slab has a thickness of 60 km with the velocity increase of 5.0%. At distances greater than 1000 km where the Juan de Fuca slab is present, the SCH-mT7 model is not fast enough to match the *P* arrivals denoted by solid black lines. Travel times are handpicked and the variance of travel-time residuals is reduced from 1.15 s (SCH-mT7) to 0.33 s (JdF10).

[18] To model *S* waveforms, we create an *S* velocity model (JdF10S) using the scaling factor $R = \delta \ln V_s / \delta \ln V_p$ and the JdF10P model. Consistent with *Sun and Helmberger* [2011], R = 2 is found to provide a good fit to most travel times (Figure 11). However, we find that locally changing the *R* value within the JdF slab provides a better fit to SH waveforms that sample the slab. After testing several *R* values between 1 and 2, we find that *R* = 1.2 for the JdF slab is optimal for fitting SH waveforms from the S1 corridor (Figure 11). Waveforms predicted by the SCH-mT7 model (scaled with *R* = 2) are also presented. We include the raypaths to indicate the sampling. Because low-velocity anomalies frame the JdF slab, the velocity contrasts reach over 8% and predict multipathed waveforms, which are apparent near 6800–6900 km in both *S* and *sS*. The change in the 1D reference causes some timing issues at the shortest distances but the SCH-mt7 model produces a remarkable match. The model JdF10S with a sharper velocity contrast does a better job at stations H08A-I09A where the multipathing from the DNTS becomes prominent. The multipathing from the DNTS is more evident along the more northern profile S2 (Figure 12). Note the low amplitude and waveform complexity near station BMO associated with the high-velocity anomaly. Again both velocity structures produce good fits except for some secondary phases between *S* and *sS* in the FD synthetics which are caused by grid issues when coupling the 1D to 2D models as discussed in Appendix A. The JdF10S velocity structure contains identical JdF slab and deep high-velocity anomaly as in Figure 11 except that the shallow tomography velocities have been changed. In particular, the S2 velocity section (Figure 12) contains a relatively fast strip from BMO to E07A. This anomaly causes the small feature near the distance of 6600 km, and explains the low amplitude as discussed earlier.

5. Oregon Corridor R2

[19] In this section, we address the data sampling northern Oregon near the Washington-Oregon border beneath Portland (Figure 3). This is an interesting sample in that the JdF slab appears to be missing at depth (Figure 2c) with only weak evidence for multipathing. Unfortunately, this profile is probably not 2D in nature and modeling becomes more of a 3D process. This region will be readdressed when data from the High Lava Plains flexible array becomes available. Here, we will simply examine the regional data from the Nevada earthquake and the two teleseismic samplings of *P* and *SH* waves (Pw2 and S3 in Figure 3). The regional waveforms appear very much like those observed along the northern profile (R1). However, the R2 profile ends before reaching 1000 km at the Oregon coastline. The timing is similar to the profile R1 along with the amplitude increase. Since the slab is closer to the event, we have moved the slab structure to the east accordingly. The preferred velocity structure JdF20P is generated in the same way as JdF10P and the comparison of the synthetics and observations is displayed in Figure 13. *P* wave recorded at the southernmost station HEBO is slightly early indicating a stronger slab southward (Figure 13c). The slab appears to be truncated at a depth of 100 km, which is determined by the teleseismic *P* wave data Pw2 as given in Figure 13. The complicated waveforms near G06A are caused by the deep high-velocity anomaly and modeled by JdF10P, although not wiggle by wiggle (Figure 13d). The travel-time derivations are not large but reasonably predicted. The corresponding *SH* waveform fits are displayed in Figure 14

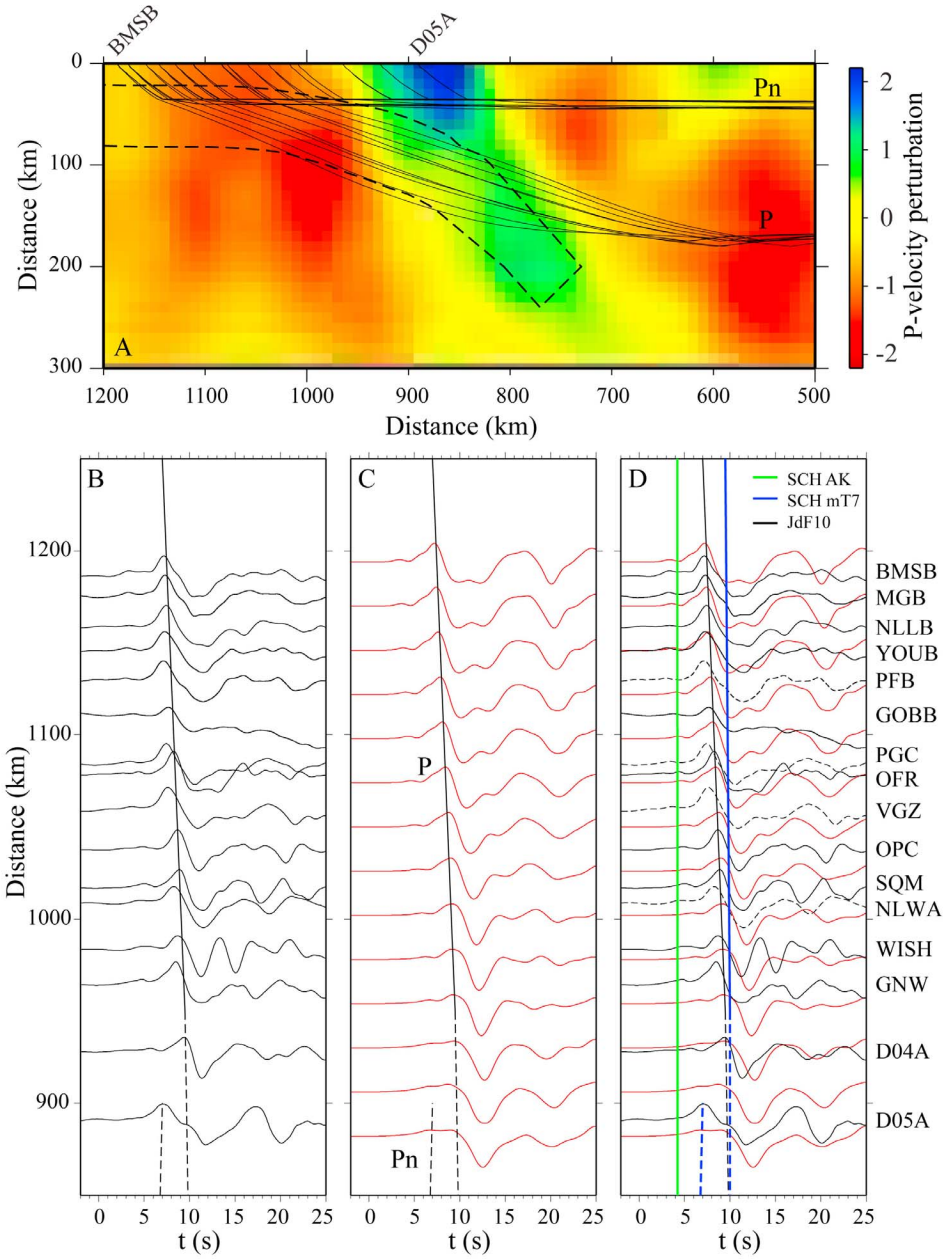

Figure 7. (a) *P* wave raypaths for stations between 850 km and 1200 km. Shallow horizontal paths are P_n waves and deeper paths are *P* arrivals. Dashed lines mark boundaries of the Juan de Fuca slab in model JdF10, while the velocity perturbations are those from the tomographic velocity model SCH. (b) Observed data (black waveforms) and (c) FD synthetics (red waveforms) of the vertical component from the Nevada earthquake are plotted on the bottom as well as (d) their direct comparison. Black lines denote *P* and P_n arrivals. Green and blue lines are arrivals from model SCH with AK135 and mT7 as background, respectively. Dashed seismograms are about 1.0 s earlier than predictions of JdF10, which could be a 3D effect of the slab because they have relative larger azimuth and perhaps longer travel in the fast slab.

with a scaling factor R = 2.0 for the JdF slab, which is quite high, consistent with warmer asthenosphere [*Cammarano et al.*, 2003] adjacent to the slab along R2. Near station J07A, the multipathing is strong in agreement with JdF20S predictions. The strong amplitude near station HOOD is produced by focusing caused by the low-velocity zone just to the east of the JdF slab, which has been discussed at length by *Xue and Allen* [2007].

[20] In summary, JdF20P is constructed following the same procedure used in modeling R1. Essentially, we use Figure 3 to set the top of the slab and adjust its depth of penetration based on modeling the two record sections, Pw2 and S3. This is achieved through a forward modeling exercise, essentially a restricted grid search that eliminates models that obviously would not work. In this sense, the

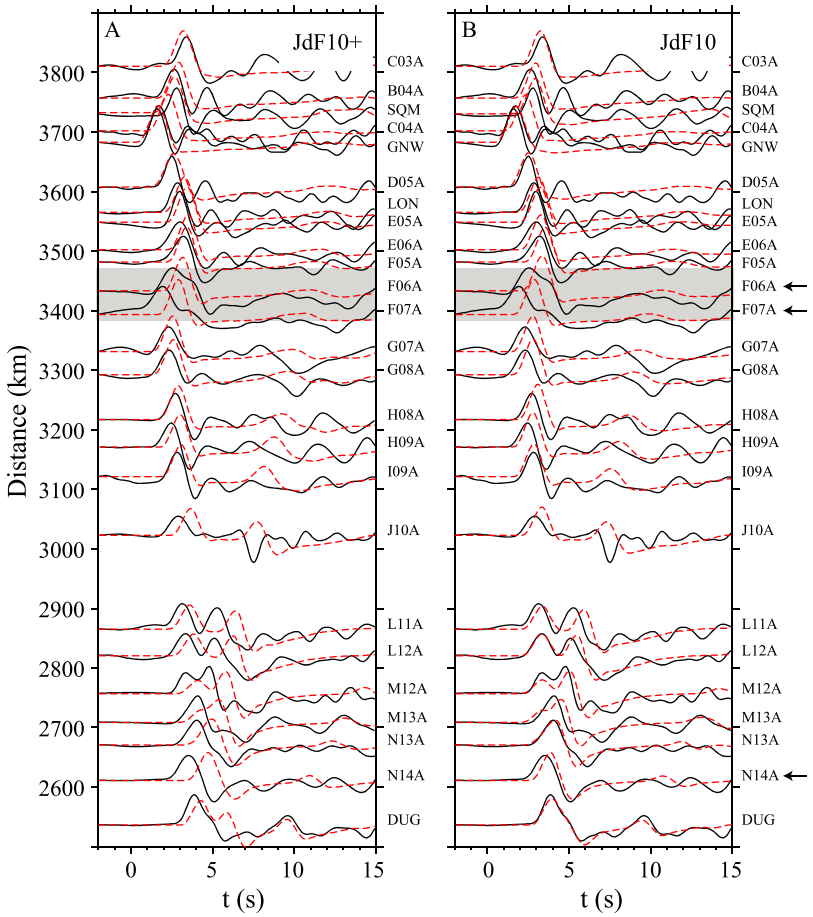

Figure 8. Comparison of observed vertical displacements (black) and WKM synthetics (red) for (a) JdF10+ and (b) JdF10 velocity models. The JdF10+ model consists of JdF10 model along with velocity perturbations below 300 km from SCH. At larger distances, these two models produce almost identical waveform fits. At distances less than 3100 km, model JdF10 fits the data better, which suggests that the deep anomalies are not important. The JdF10 synthetics are shifted back 0.4 s to compensate for delays produced by the fast anomalies below 300 km. The shaded area shows multipathed waveforms, which are caused by the Deep Nevada Transition Structure (DNTS).

procedure is similar to simulating annealing, in that it is stochastic but preferentially samples values near the optimal value from the previous iteration rather performing an exhaustive grid search. We will attempt such an inversion in future efforts. However, at this stage, we simply demonstrate model usefulness by predicting waveform data, as discussed in Appendix B.

6. Discussion

[21] The western United States (WUS), starting at the Rocky Mountain Front, provides an overwhelming contrast in tectonic style compared to the simplicity of plate tectonics in the Pacific Basin. While the upper mantle structures beneath the Pacific Basin appear rather simple even with the addition of USArray data [*Liu et al.*, 2011], WUS mantle structure has become increasingly complex. We pick two tomography models that agree quite well and are in general agreements with results from our waveform modeling. They are presented in Figure 15, namely, the *P* velocity SCH images (top left) and the *SH* velocity images by *Tian et al.* [2009] (top right). The SCH images are derived from classical teleseismic tomography assuming a global 1D reference AK135. The SCH images use more teleseismic data for travel-times measured in multiple frequency bands and have strong anomalies with relatively sharp edges. These anomalies are sharp enough to make teleseismic paths deviate from assumed tomographic raypaths and produce waveform complexities as discussed earlier. This indicates that, in this region, travel times alone can predict some of the focusing and defocusing features that are observed in waveform data. The second tomographic images include multifrequency *SH* travel-time and amplitude data and is a step closer to actually modeling of waveforms. *Tian et al.* [2009] demonstrate that velocity heterogeneity can dominate seismic attenuation and that observed amplitudes can be used directly to improve tomographic images of velocity. This concept is validated here in that we find the tomographically imaged low-velocity anomalies produce larger amplitude arrivals. In Figure 15 we compare the two models and our hybrid our hybrid structures JdF10P and JdF20P along the same corridors. We suggest that there is a kink in

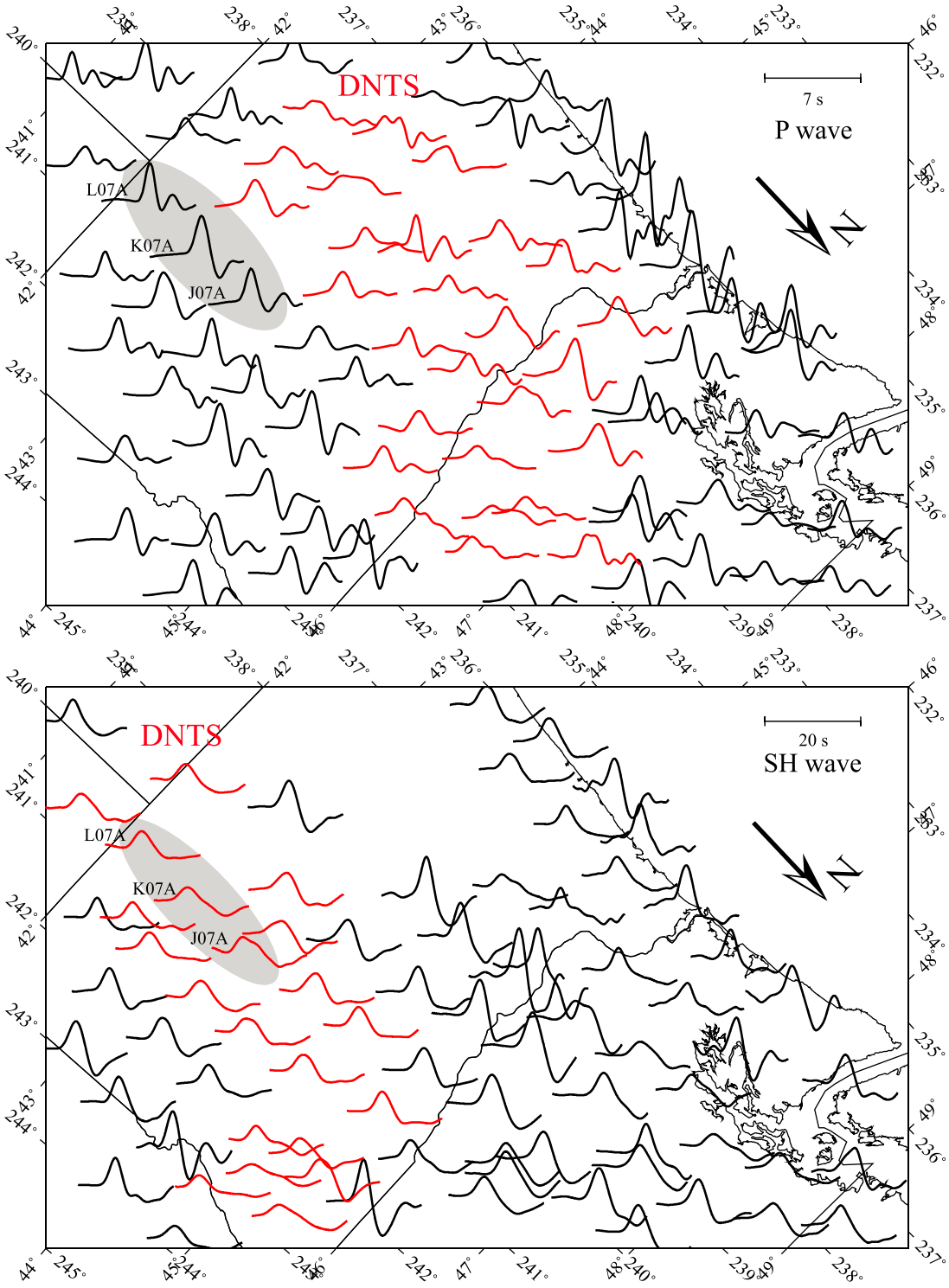

Figure 9. *P* and *SH* waveform complexities for (top) the 2007 Gulf of Mexico earthquake and (bottom) the 2007 South America event. Red traces have lower amplitudes and complex waveforms, which appear to be multipathing caused by the DNTS. Note that the complexity is along a 3° strip in the top panel. Because the South America earthquake has larger distances and smaller incident angles, the multipathing effects appear closer to the anomaly as denoted by the shaded ellipse of observations at stations J07A, K07A, and L07A. Later we back-project these patches along raypaths to that multipathing caused by the DNTS is a likely origin (Figure 16).

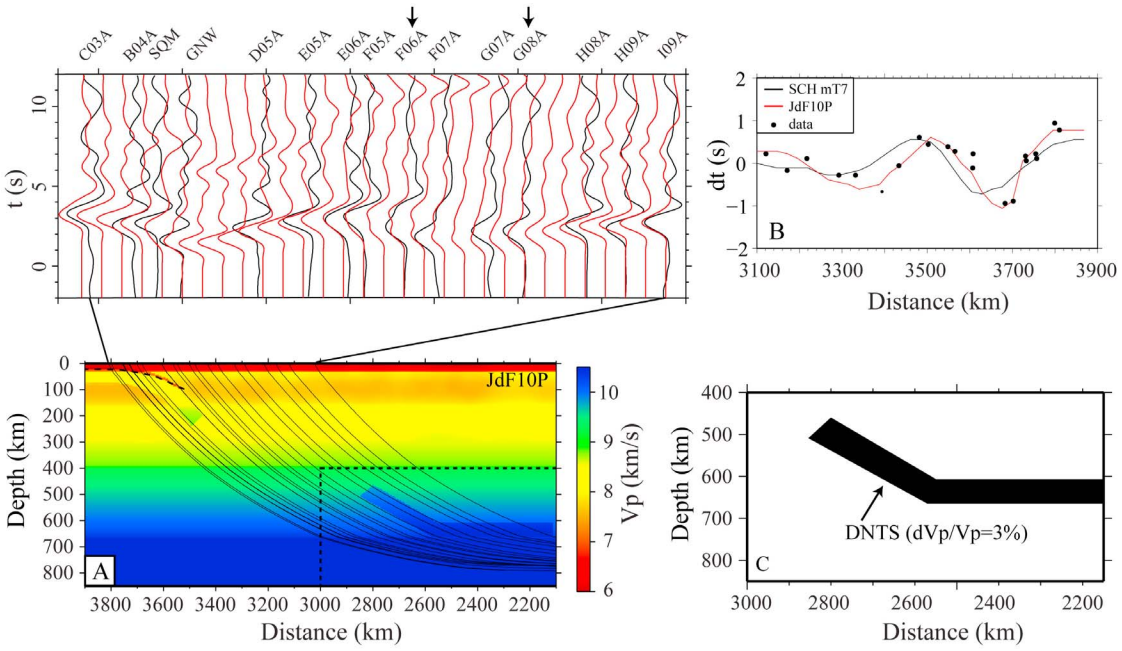

Figure 10. Waveform fits for the profile Pw1. (a) Comparison of observed (black) vertical displacement and FD synthetics (red) for *P* velocity model JdF10P with *P* wave travel-time residuals for SCH-mT7, JdF10P, and (b) data are displayed. The variance of travel-time residuals is reduced from 0.17 s (SCH-mT7) to 0.04 s (JdF10P). (c) The *P* velocity variation along the profile is given in absolute levels with the DNTS displayed as velocity perturbations.

the slab structure between these two corridors where the northern section strikes more to the east along the eastern edge of the Cascades (Figure 2b). This kink could be related to rupturing of the slab around the time of the Miocene Columbia River Basalts (CRB) eruptions (∼17 Ma), and there is strong evidence for a low-velocity structure below this region (Figure 2). Some stations, i.e., HOOD (Figure 3), have very large amplitudes, which when migrated downward hit the very slow region in both models near the southwestern edge of where the CRB erupted. Moreover, both models display an absence of slab below a depth of 200 km near Corridor II. This feature is reinforced by our waveform modeling using regional data exclusively, which removes any issue about vertical smearing. However, to model the strength and timing of the P_n to *P* transition requires a large velocity contrast, in particular a *P* velocity of 8.2 km/s with the geometry displayed for both corridors averaged over the slab thickness of 60 km. Modeling the teleseismic *SH*-data with this geometry provides an estimate of 4.5 km/s for Corridor R1, or an R = 1.2, to the north, which may indicate relatively cool temperatures in the northern part of the Cascadia wedge.

[22] To the south, the R estimate for Corridor II is 2.0. This is a high value and indicative of high temperature and perhaps some melt as discussed in the work of *Schmandt and Humphreys* [2010]. The high R value is consistent with a hot zone near the Oregon-Washington border with temperature elevated by about 100°C to 300°C [*Xue and Allen*, 2007]. Both teleseismic tomography images have a very low-velocity zone at this location consistent with our regional waveform modeling. The above values for plate thickness of 60 km is in agreement with a 10 Ma year old plate from modeling multiple *SH* data along the East Pacific Rise [*Melbourne and Helmberger*, 2002] and the Pacific-North America margin study [*Melbourne and Helmberger*, 2001]. They also found an *S* wave velocity of 4.5 km/s for the lid as the oceanic plate approaches the continent along the San Andreas Fault system. Thus, it appears that the Pacific plate is strong and probably modulates the long-term weak continental deformations. Near the CRB region, there appears to be a window where the LVZ extends from beneath the Pacific into the northern Basin and Range. Inflow of warm Pacific asthenosphere could provide extra heat to drive intraplate deformation and volcanism.

[23] The velocity anomalies in our hybrid structures are more extreme compared to tomography and the shape of the JdF slab looks more like a subducted slab produced by numerical convection modeling, e.g., *Liu and Gurnis* [2008]. In particular, dynamic modeling studies of the ridge-trench collision by *Burkett and Billen* [2010] have shown that ridge-trench collision may produce shallow detachments for tectonic settings similar to the Cascadia subduction zone, which is very close to the Juan de Fuca ridge. They also suggest that upward flows along the edges of the slab both toward the ridge and in board are likely, which could help explain the observed multipathing by introducing strong low-velocity anomalies adjacent to the high-velocity slab. As data sets from the flexible arrays, such as High Lava Plains Network, become available, the relatively simple models presented here will probably become more 3D and both adjoint waveform modeling and dynamic modeling can be attempted. Previous dynamic-modeling attempts using present tomographic images proved unsuccessful because weak structures rapidly dissipate. Thus

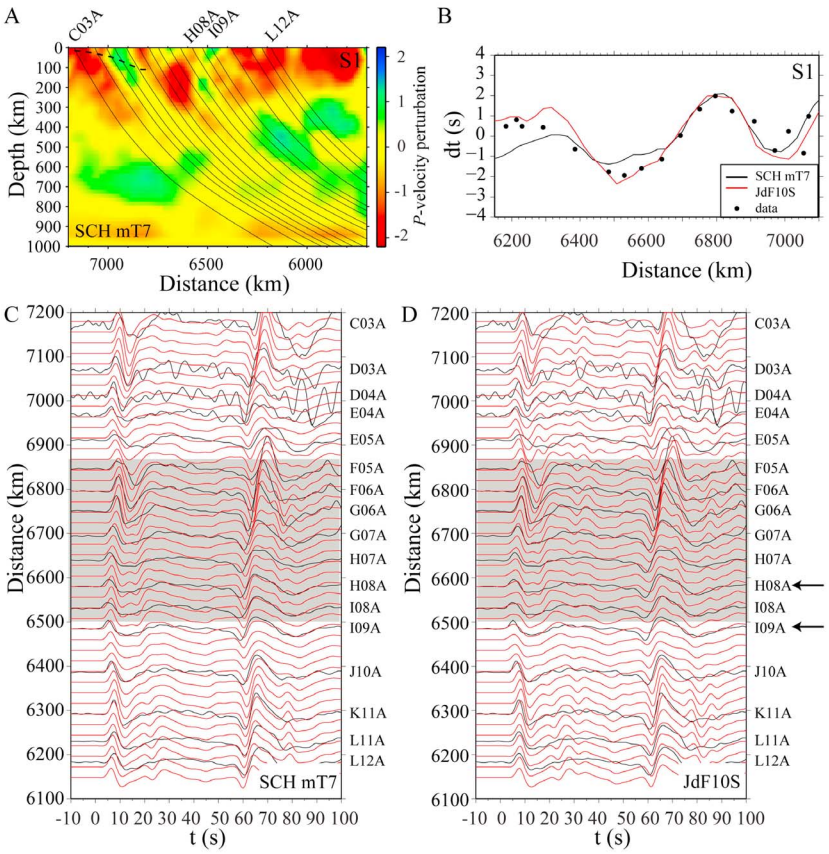

Figure 11. Waveform fits for the profile S1. (a) The *P*–wave tomographic image from SCH with WKM raypaths displayed along with a dashed line indicating the upper slab edge. (b) *S* wave travel-time residuals from the South American earthquake for model SCH with mT7 as background (black line), JdF10S (red line), and observed data (black dots). The variance of travel-time residuals is reduced from 0.54 s (SCH-mT7) to 0.34 s (JdF10S). Comparison of observed and FD synthetic horizontal displacement for these two models is displayed (Figures 11c and 11 d, respectively). In order to construct *S* wave velocities of SCH-mT7, we assume a uniform ratio $R = \delta \ln V_s / \delta \ln V_p = 2.0$. The model JdF10S has the same R ratio except that R is 1.2 and 2.3 for the JdF slab and DNTS with respective to model JdF10P, respectively. Note the improvement of travel-time fits displayed in shaded area.

sharper velocity contrasts are needed to produce dynamic stability [*Liu and Gurnis*, 2008]. Our results demonstrate that waveform modeling applied to a few key events can help determine whether tomography structures are robust and whether they require modification such as amplification or sharpening of edges. This is especially important for weak structure below 300 km (Figure 15).

[24] Defining the seismic structure at greater depths proves difficult because high-resolution methods need to rely on shallow velocities for migrating and results differ [*Cao and Levander*, 2010]. Here in Figure 16a, we display receiver function images from stacking USArray data assuming the *Sigloch et al.* [2008] velocity structure although other velocity structures produce similar results with the strongest "410" elevation occurring beneath Northern Nevada. They attribute the elevated "410" discontinuity to a change of water content caused by possible slab dehydration. A deflection of the "660" discontinuity beneath Utah supports this interpretation, but again this result depends on the migration issues. We have back-projected our multipathing results along raypaths to a depth of 410 km, and find good agreement with both models. The *Tian* model also shows the detachment, DNTS, flattening-out just above the "660" discontinuity similar to that displayed in Figure 10.

[25] The fate of slabs encountering the "660" has long been a topic of interest. The latest integrated thermodynamic-mineralogical modeling, suggests that they should penetrate unless they encounter this density barrier at angles less than 40° [*Ganguly et al.*, 2009]. Thus, the details of such structures become essential information for understanding both tectonics and earth structure. We will attempt to sharpen this image by adding triplication data sampling the transition zone at this location in future efforts.

7. Conclusions

[26] We presented seismic velocity structures of the Juan de Fuca slab along two corridors using a mixture of tomographic features, a priori constrains on slab geometry, and waveform modeling. The *Schmandt and Humphreys* [2010] tomographic images are used as the starting structures after

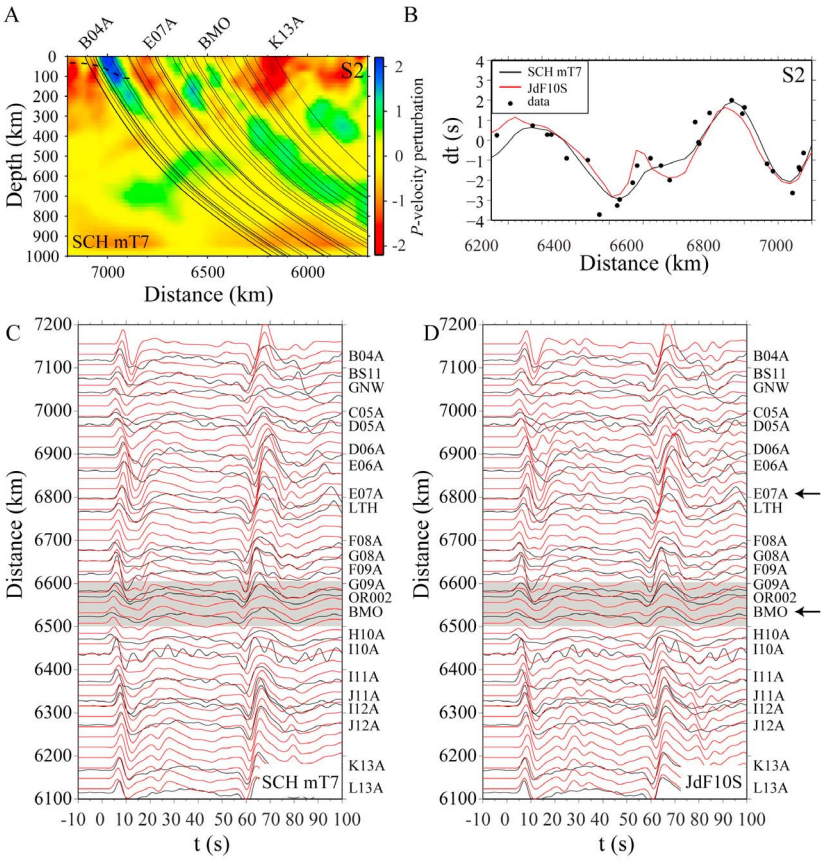

Figure 12. Waveform fits for the profile S2. (a) The *P*–wave tomographic image from SCH with WKM raypaths displayed with station identifications. (b) *S* wave travel-time residuals from the South American earthquake for model SCH with mT7 as background (black line), JdF10S (red line), and observed data (black dots). For stations shown in shaded box, our model predicts the early arrival caused by the DNTS. Comparison of observed (black) and FD synthetic (red) horizontal displacement for these two models is displayed (Figures 12c and 12 d, respectively). The Juan de Fuca slab has the same structure of S1. See Figure 11 for more details. Note the improvement of travel-time and waveform fits displayed in shaded area.

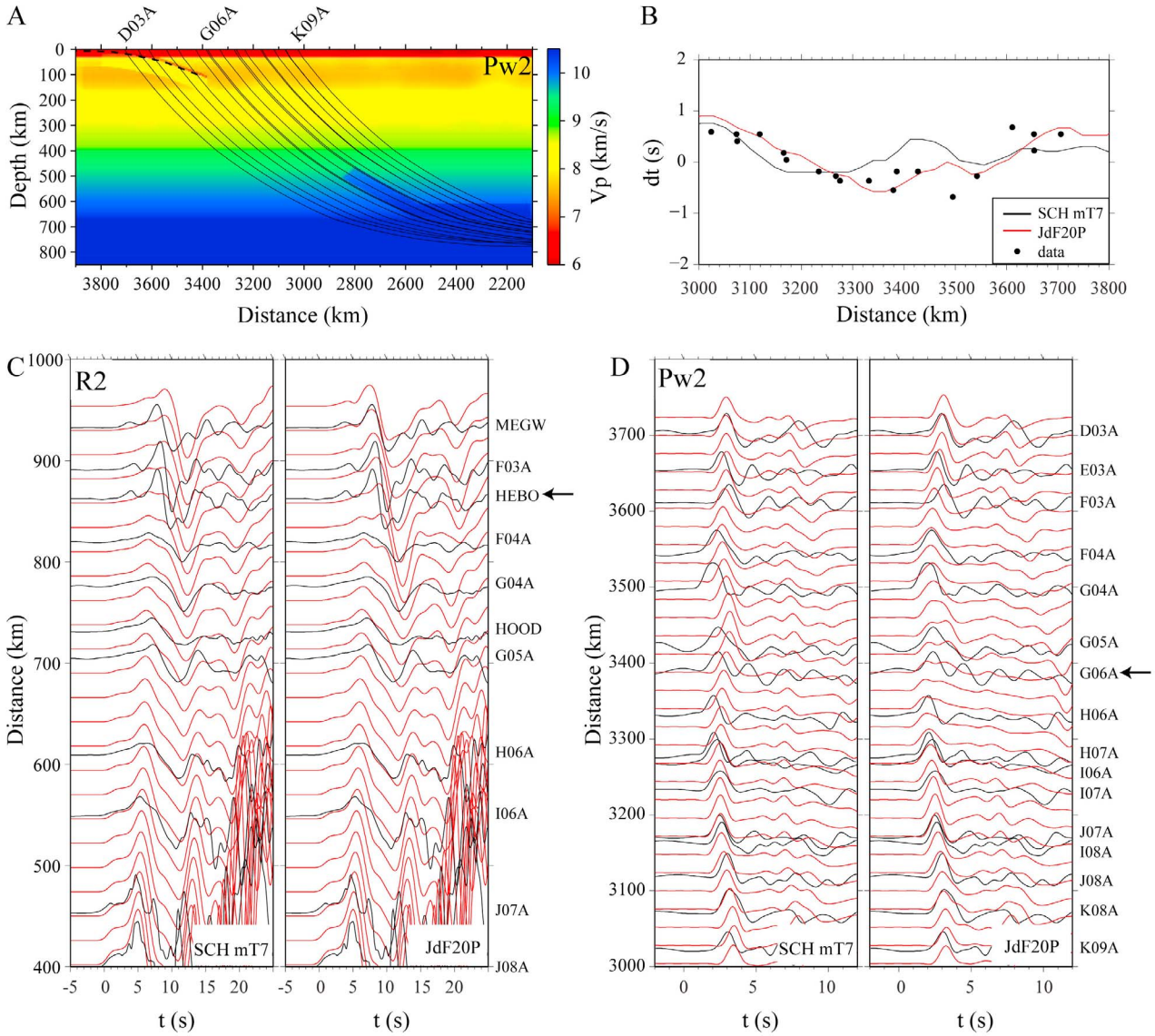

Figure 13. Waveform fits for the profile Pw2. (a) *P* velocity model JdF20P along profile Pw2 is shown in absolute values with WKM raypath. (b) *P* wave travel-time residuals for SCH-mT7 (black line), JdF20P (red line), and data (black dots). The variance of travel-time residuals is reduced from 0.15 s (SCH-mT7) to 0.06 s (JdF20P). (c) Comparison of vertical displacement data (black) and FD synthetics (red) for profile R2 using velocity model SCH-mT7 (left) and Jd20P (right). (d) Comparison of vertical displacement data (black) and FD synthetics (red) for profile Pw2 using velocity model (left) SCH-mT7 and (right) Jd20P. The Juan de Fuca slab is about 110 km deep, as shown in Figure 2c.

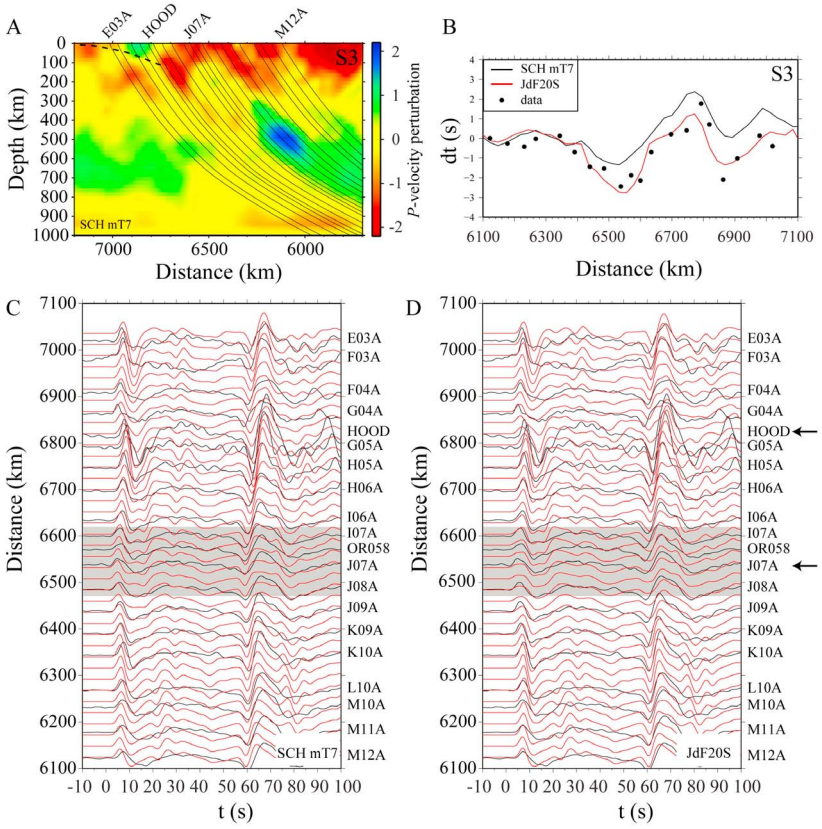

Figure 14. Waveform fits for the profile S3. (a) The *P*–wave tomographic image from SCH along profile S3 with WKM raypaths displayed. (b) *S* wave travel-time residuals from the South American earthquake for model SCH with mT7 as background (black line), JdF10S (red line), and observed data (black dots). The variance of travel-time residuals is reduced from 0.46 s (SCH-mT7) to 0.33 s (JdF20S). Comparison of observed (black) and synthetic (red) horizontal displacement for these two models is displayed (Figures 14c and 14 d, respectively). Note the improvement of travel-time and waveform fits displayed in shaded area. The JdF20S has R ratio at 2.0 for the Juan de Fuca slab and 2.3 for the DNTS. See Figure 11 for more details.

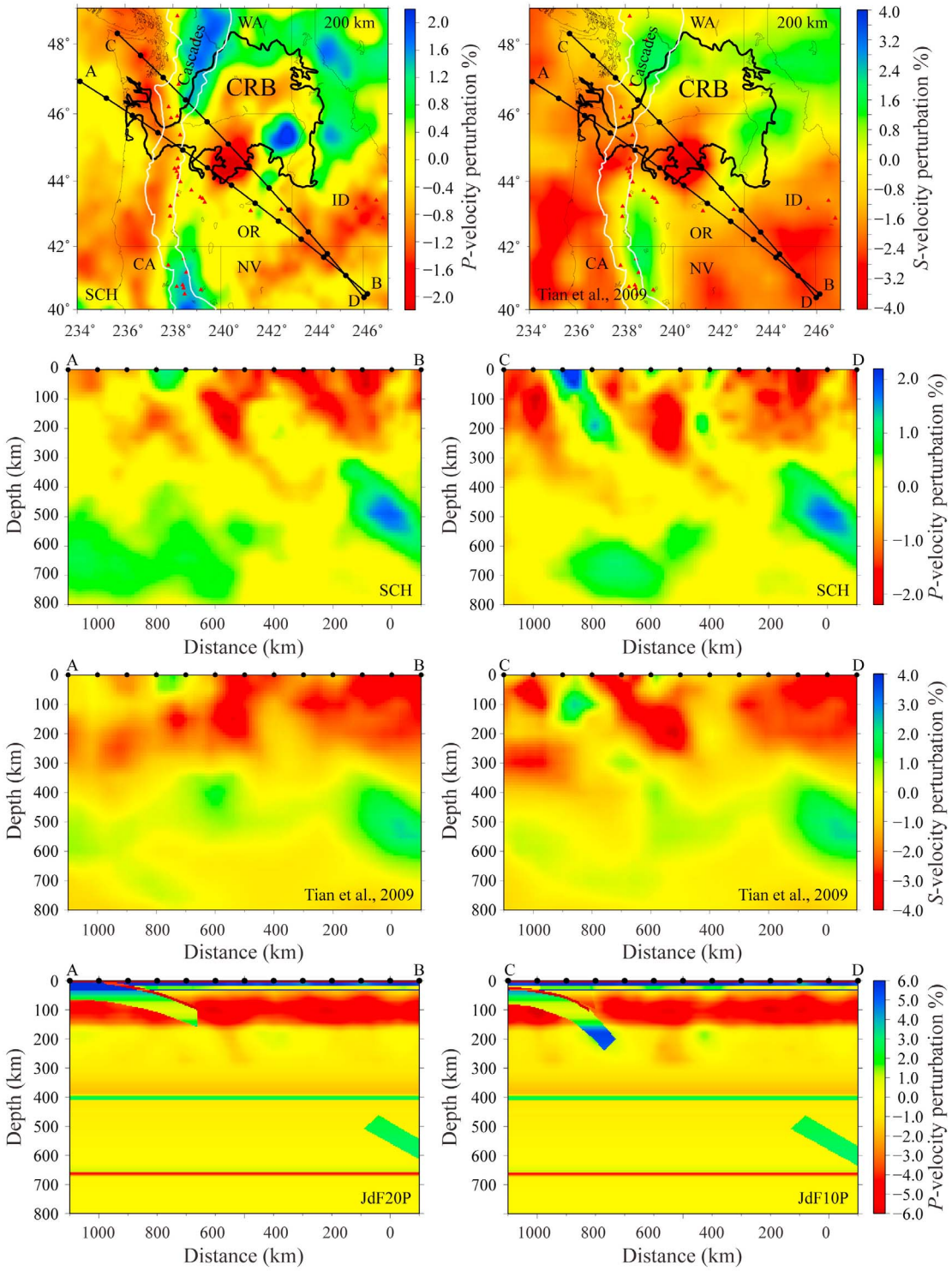

Figure 15. Comparison of velocity profiles along corridors (left) AB and (right) CD with respect to AK135 for *Schmandt and Humphreys* [2010], *Tian et al.* [2009], and JdF10P and JdF20P. The location of AB and CD are displayed with the tomography map at 200 km on the top. White lines mark the boundary of the Cascades and thick black lines denote the boundary of the Columbia River Basalts (CRB). Red triangles represent volcanoes in the western United States. The lower panels display the velocity images for *P* waves (SCH), *SH*-waves (Tian), and at the bottom, our hybrid model JdF10P and JdF20P. The SCH anomalies below 300 km are not needed to match this data set.

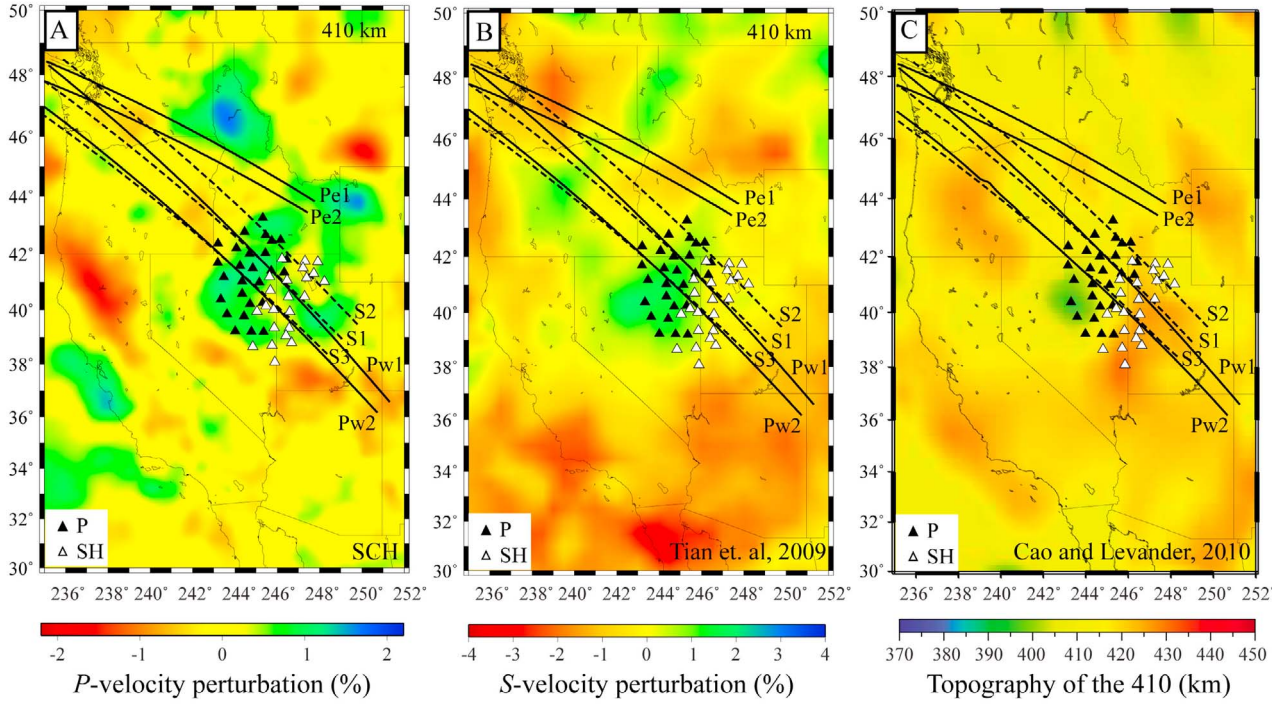

Figure 16. Seismic stations with complex *P* (black triangles) and *SH* (white triangles) waveforms (red in Figure 9) are migrated down to 410 km along raypaths from these two events assuming a 1D model mT7, and displayed relative to the seismic tomography from (a) *Schmandt and Humphreys* [2010], (b) *Tian et al.* [2009], and (c) receiver function stacking [*Cao and Levander*, 2010]. Solid and dashed lines are *P* and *SH* profiles we modeled in this study.

changing their 1D reference from AK135 to mT7, a modification of the older Basin-and-Range model T7. Model mT7 has a well-developed low-velocity zone similar to TNA, more compatible with the Pacific Basin models. Synthetics produced by mT7, containing the crossover from P_n to *P* at ranges 650 to 1200 km, do not match the seismic data from regional earthquake in Northern Nevada. Inserting a 60 km slab with a *P* velocity of 8.2 km/s enclosed in an envelope of low-velocity structures provides synthetics that can match the regional waveforms (Figure 6). The slab penetrates to a depth of about 250 km beneath the Seattle region while terminating at a shallower depth beneath the edge of the CRB near the Washington-Oregon border. Synthetics produced by these new slab structures fit teleseismic *P* and *SH* waveforms and travel times with *S* wave velocities of 4.5 km/s for the northern corridor and 4.3 km/s for the southern corridor. The southern corridor has a relatively strong low-velocity zone that extends into the upper mantle and provides larger amplitudes near the station HOOD (Figure 3). Suppressing the tomographic velocity perturbations below 300 km has a negligible effect on the waveform along both corridors although they may be needed for other profiles. A deep high-velocity anomaly beneath Northern Nevada is required to explain strong multipathing in both *P* and *SH* waveforms (Figures 11–14). The deep anomaly has larger velocity perturbations than imaged by tomography. We find that anomalies of +3% for *P* and +7% for *SH* are consistent with body wave amplitudes and multipathing as well as travel-time measurements typically used in mantle tomography. Additionally, such a deep cold structure is confirmed by stacked receiver functions [*Cao and Levander*, 2010], and higher mode surface-wave modeling [*van der Lee and Nolet*, 1997].

Appendix A: Waveform Simulations

[27] There are many commonly used methods for computing synthetic seismograms, which can be divided into two categories: numerical and analytical. With modern parallel computing, both 2D finite difference method (FD) and 2D/3D spectral-element method (SEM) can be used to generate synthetics [*Helmberger and Vidale*, 1988; *Komatitsch and Tromp*, 1999]. The FD method simulates *P-SV* and *SH* motions separately by expanding the exact 3D solution into asymptotic forms. Analytical Cagniard-deHoop solutions are used to load the FD source excitation [*Helmberger and Vidale*, 1988]. *Chen et al.* [2007] used this method to develop 2D models of the slab structure beneath Japan and then test these results against 3D SEM synthetics. These two methods produce nearly identical waveforms validating the 2D FD. The 2D approach can be expanded to simulate 3D features by applying diffraction operators [*Helmberger and Ni*, 2005] and applied to regional modeling [*Song and Helmberger*, 2006].

[28] Analytical or ray-based methods, such as WKBJ, require smooth structures. An advantage of the ray-based method is that the raypaths indicate what portion of the model is being sampled. The WKM method [*Ni et al.*, 2003] used here generates raypaths, which automatically display the sampling region (Figure A1) and can be applied directly

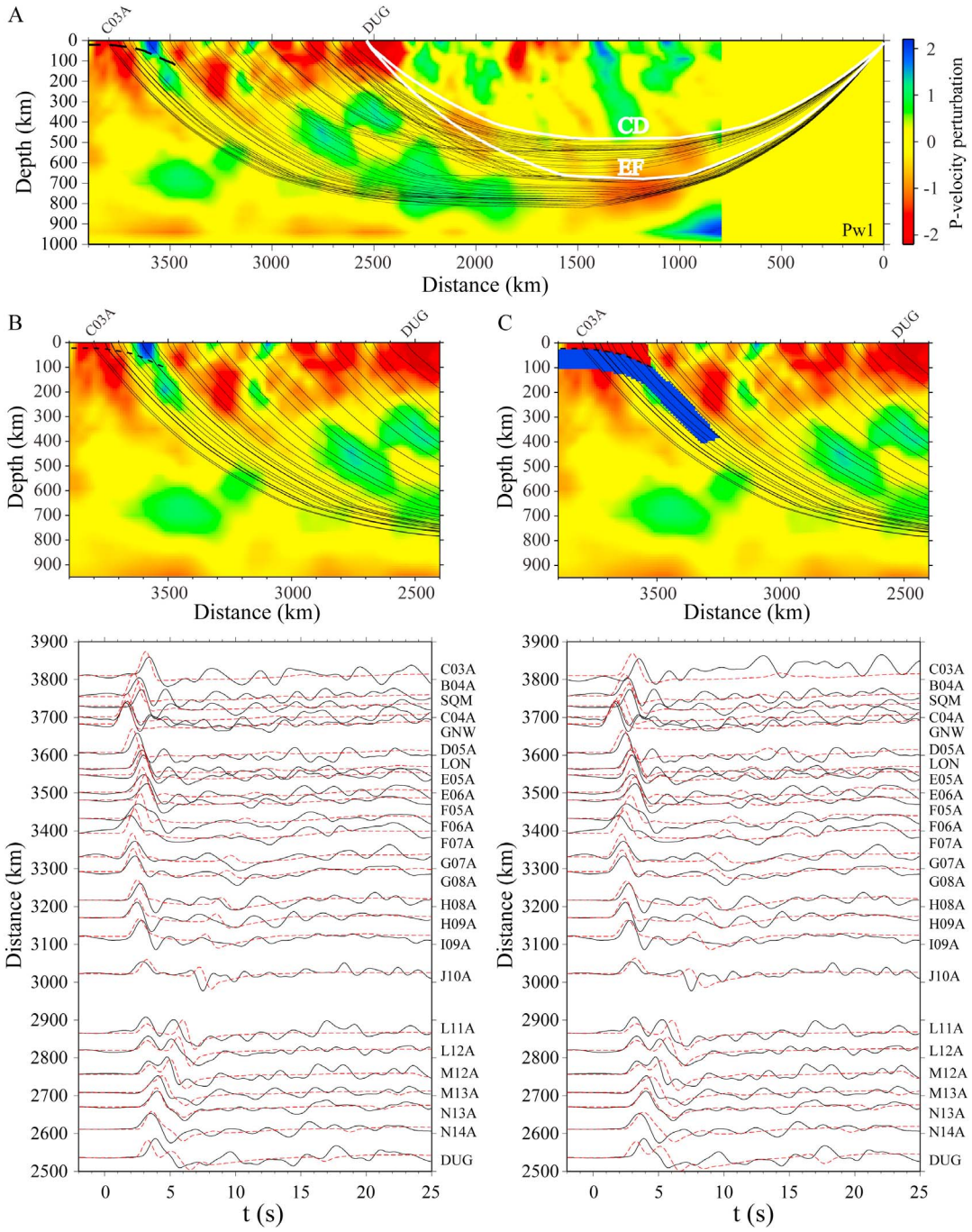

Figure A1. Velocity perturbations from SCH and raypaths along the profile Pw1 for the 2007 Gulf of Mexico earthquake (Figure 3). The raypaths are calculated using the WKM method. Raypaths below Pw1 are plotted in the middle. The Juan de Fuca slab can be replaced by a slab with a thickness of 80 km and velocity increase of 2.0%. Waveform fits for these two velocity models are displayed below.

to existing tomographic models. The method has been benchmarked against the 2D pseudo-spectral [*Ni et al.*, 2003] and 3D SEM methods [*Ni et al.*, 2005] for deep earth structure.

[29] The raypaths displayed in Figure A1 are produced by a two-step process. First, a 1D model is divided into layers and ray segments defined by ray reflections from each interface. Those raypaths nearest to the geometric arrivals are approaching the critical angles and are mostly controlling the response [*Chapman*, 2004]. Next we add velocity perturbations obtained from tomography and adjust the ray segments to satisfy Snell's Law. Ray segments with increased velocities are lengthened relative to decreased velocity regions. These are the paths displayed in Figure A1a. Note that at distances less than about 3000 km (27°), two paths are possible indicating a triplication with the two

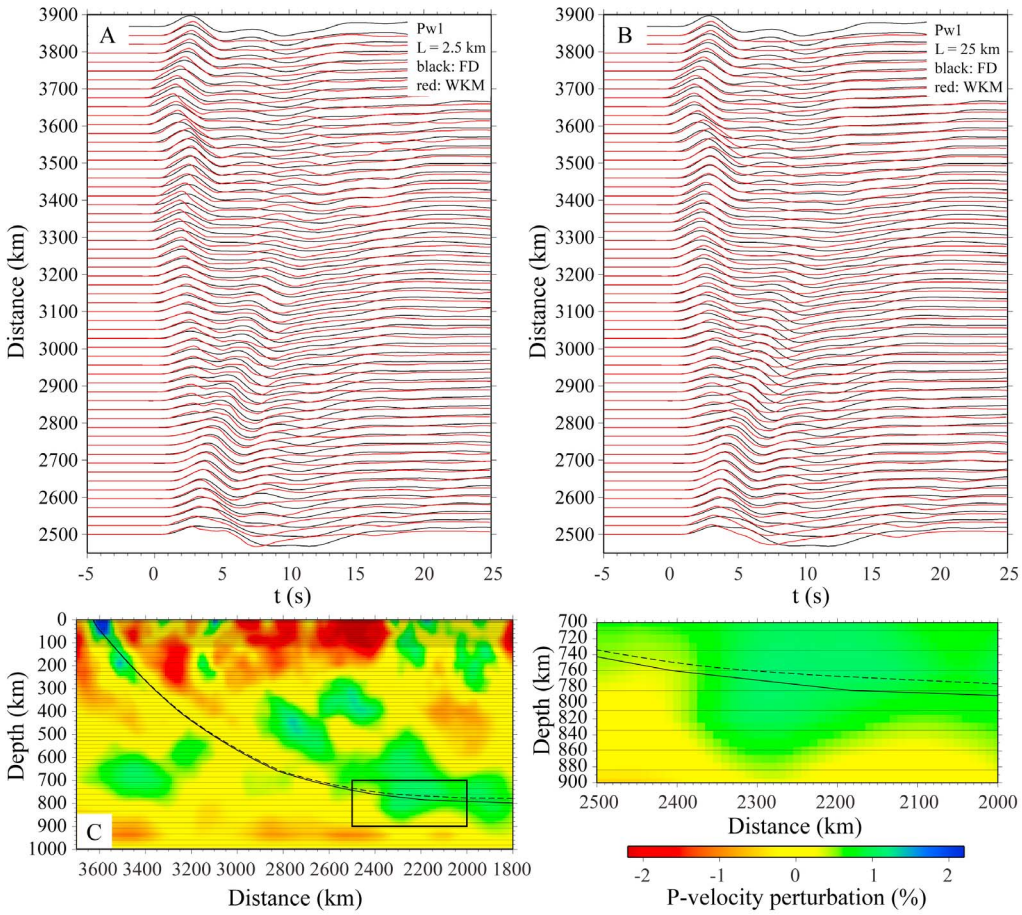

Figure A2. Comparison of synthetic seismograms from FD (black) and WKM (red). The finite difference calculation has a grid size of 2 km. The WKM synthetics have different layer thicknesses of (left) 2.5 km and (right) 25 km. Dashed and solid raypaths are for layer thickness of 2.5 km and 25 km for a station above the Juan de Fuca slab. The paths in the box are enhanced on the right displaying the sensitivity to layering.

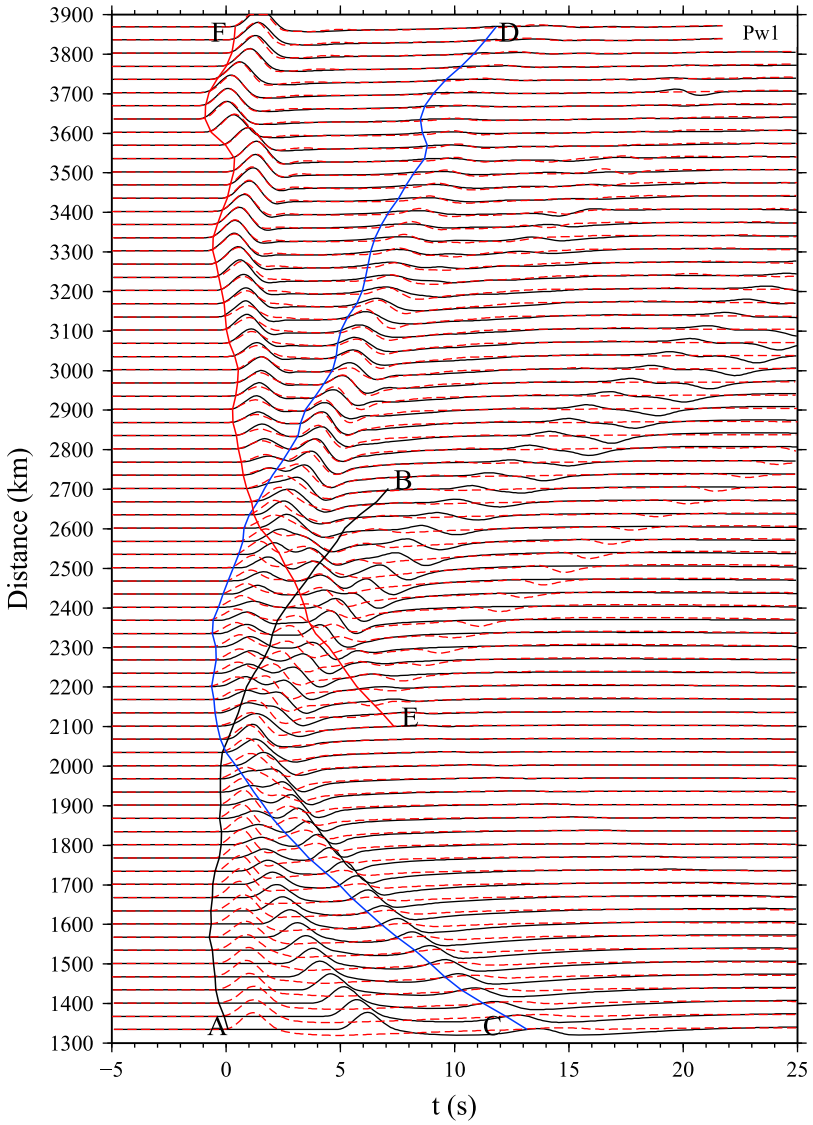

Figure A3. Comparison of synthetic seismogram using AK135 (red) and mT7 (black) as background velocity model for profile Pw1. The synthetics are aligned relative to AK135, i.e., if the tomographic is suppressed, the first arrivals would be a straight line. Red waveforms are shifted by 1.9 s. In these calculations, we use the velocity perturbations $\Delta V/V$ from SCH. The change of background model has little effect on waveforms and relative arrival times for teleseismic arrivals. However, arrival times are sensitive to the background model at regional and upper mantle distances. AB, CD and EF are triplicated arrivals, which turn above the 410 discontinuity, in the transition zone, and below the 660 discontinuity. Black, blue and red lines indicate arrival times of AB, CD and EF, respectively.

forward branches denoted, EF and CD. These locations produce two arrivals as displayed in the comparison of synthetics with data from the Gulf of Mexico event (Event Pw in Table 1). The early arrivals near station C04A are obvious as well as the late arrivals near E06A and well modeled by the SCH model. Since the event is outside the seismic network, the approach used here simply applies a base-line shift moving the seismic section forward or backward to match the record section, *VanDecar and Crosson* [1990]. In Figure A1c, we included a preliminary run by imposing a slab. As expected, one can easily modify existing tomographic models in order to model waveforms. However, mixing sharp structures with smooth tomography causes difficulties with ray tracing and it becomes important to test the models against numerical simulations. The results of such a test are given in Figure A2 for the SCH model. The black traces are the FD-results assuming a 2.0 km grid. The red traces are the WKM results assuming a layer thickness of 2.5 (Figure A2, left) and 25 km (Figure A2, right). Figure A2 (bottom) displays the differences for an example raypath sampling the slab. Fast zones tend to flatten rays as easily observed for the thick layers. However, since triplications have relatively sensitive geometry, small shifts in raypaths can cause changes in focusing. Generally,

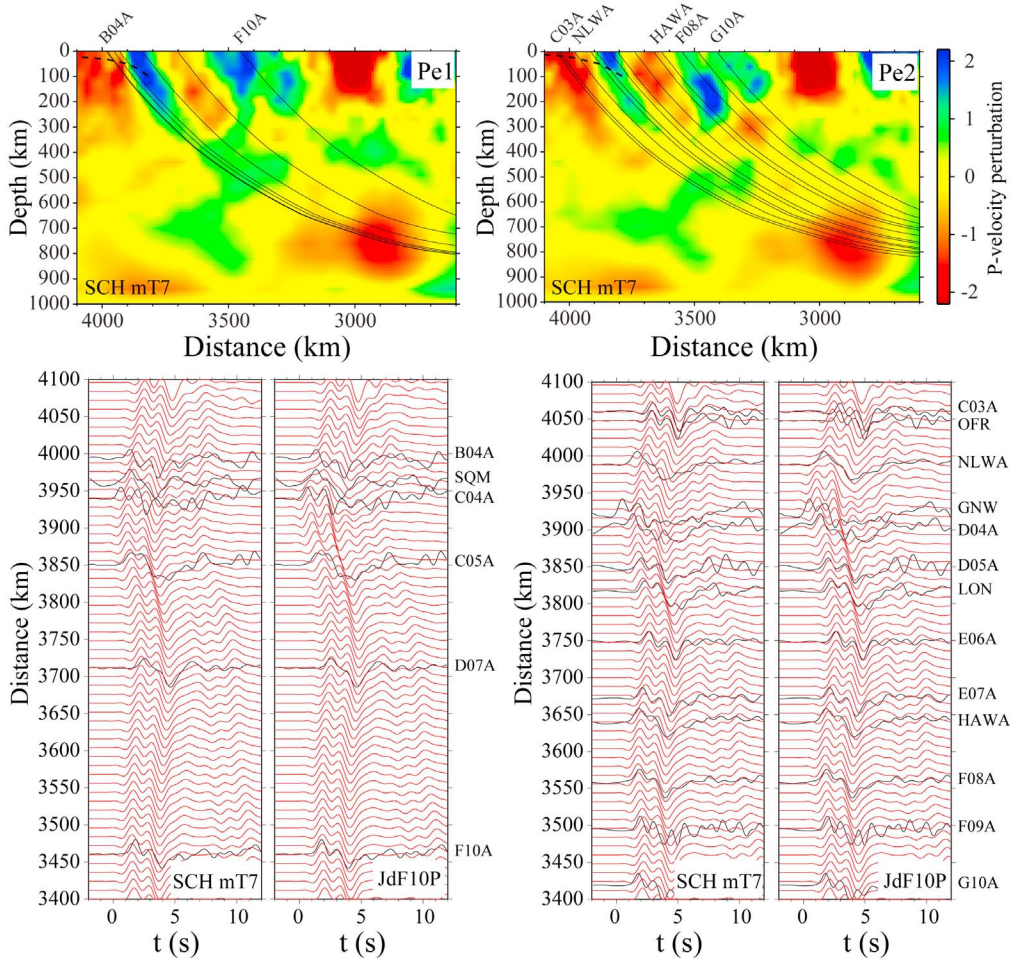

Figure B1. Comparison of data and synthetics for profile (left) Pe1 and (right) Pe2. Velocity perturbations and raypaths from SCH-mT7 are plotted on the top. Since these two profiles sample different shallow structures, velocity models here are constructed by using top 300 km of *Schmandt and Humphreys* [2010] and replacing the Juan de Fuca slab using the slab from JdF10. To account for the 3D effect, the slab along the Pe2 profile is shortened by 70 km.

it is difficult to distinguish the difference in synthetics when the layer thickness is less than 10 km, and FD and WKM produce similar triplication synthetics for smooth models.

[30] In Figure A3, we display the effects of changing the reference model for the same 2D cross section studied above. Replacing AK135 with mT7 causes a 1.9 s timing shift applied to the section determined by the upper set of seismograms. The synthetics are similar for this distance range. However, at shorter distance, the synthetics fall behind because of the slower mT7 reference model as expected. At distance less than 1300 km, the difference can reach 10 s as discussed in the section of regional modeling of Corridor I (Figure 5).

Appendix B: Validation of Corridor I

[31] A particularly important issue in modeling is the complexity caused by in-plane or out-of-plane multipathing or 2D versus 3D. It appears that the slab has a break between Corridor I and II and Corridor I is the closest to in-plane or 2D in nature. To further test this hypothesis, we add two more *P* wave sections from an event coming from the eastern Gulf of Mexico, Pe1 and Pe2 (Table 1). We use the same JdF10 model to model these record solutions displayed in Figure B1. The tomographic cross sections (SCH) are included. Note that even though these sections are less than a degree apart, the models are different.

[32] Both sections sample the fast zone near the Washington-Oregon-Idaho intersection (Figure 2c) which gets stronger toward the North. The structure is included in JdF10 which contains SCH above 300 km. This fast structure is needed to explain the early arrival near station F08A and is also a zone of significant multipathing (DFS) in *SH* waveforms (Figure 2a). There is an observed small distortion near station HAWA but the strongest multipathing occurs near NLWA apparently caused by the JdF slab structure. The JdF10 synthetics are a bit early near OFR where the fit is better using the original SCH model. The tomographic

structure below 300 km does not appear significant in these sections. JdF10 does well with just the 1D mT7 model. This record section no longer contains the DNTS complexity, which was apparent in the earlier section.

[33] **Acknowledgments.** We would like to thank L. Boschi, two anonymous reviewers, the Associate Editor, and especially the Editor Robert Nowack. Their suggestions and comments made significant improvements to the manuscript. Comments from Erin Burkett and Mike Gurnis were greatly appreciated. Seismic data were obtained from IRIS data management center. This work was supported by National Science Fundation through grant EAR-0639507 and the Caltech Tectonic Observatory. Contribution number 10060 of the Seismological Laboratory, California Institute of Technology.

References

Boschi, L., C. Faccenna, and T. W. Becker (2010), Mantle structure and dynamic topography in the Mediterranean Basin, *Geophys. Res. Lett.*, *37*, L20303, doi:10.1029/2010GL045001.

Burdick, L. J., and D. V. Helmberger (1978), The upper mantle *P* velocity structure of the western United States, *J. Geophys. Res.*, *83*, 1699–1712, doi:10.1029/JB083iB04p01699.

Burdick, S., C. Li, V. Martynov, T. Cox, J. Eakins, T. Mulder, L. Astiz, F. L. Vernon, G. L. Pavlis, and R. D. van der Hilst (2008), Upper mantle heterogeneity beneath North America from travel time tomography with global and USArray Transportable Array data, *Seismol. Res. Lett.*, *79*, 384–392, doi:10.1785/gssrl.79.3.384.

Burkett, E. R., and M. I. Billen (2010), Three-dimensionality of slab detachment due to ridge-trench collision: Laterally simultaneous boudinage versus tear propagation, *Geochem. Geophys. Geosyst.*, *11*, Q11012, doi:10.1029/2010GC003286.

Cammarano, F., S. Goes, P. Vacher, and D. Giardini (2003), Inferring upper-mantle temperatures from seismic velocities, *Phys. Earth Planet. Inter.*, *138*, 197–222, doi:10.1016/S0031-9201(03)00156-0.

Cao, A., and A. Levander (2010), High-resolution transition zone structures of the Gorda Slab beneath the western United States: Implication for deep water subduction, *J. Geophys. Res.*, *115*, B07301, doi:10.1029/2009JB006876.

Chapman, C. H. (2004), *Fundamentals of Seismic Wave Propagation*, 608 pp., Cambridge Univ. Press, New York, doi:10.1017/CBO9780511616877.

Chen, M., J. Tromp, D. Helmberger, and H. Kanamori (2007), Waveform modeling of the slab beneath Japan, *J. Geophys. Res.*, *112*, B02305, doi:10.1029/2006JB004394.

Ganguly, J., A. M. Freed, and S. K. Saxena (2009), Density profiles of oceanic slabs and surrounding mantle: Integrated thermodynamic and thermal modeling, and implications for the fate of slabs at the 660 km discontinuity, *Phys. Earth Planet. Inter.*, *172*, 257–267, doi:10.1016/j.pepi.2008.10.005.

Gao, W., S. P. Grand, W. S. Baldridge, D. Wilson, M. West, J. F. Ni, and R. Aster (2004), Upper mantle convection beneath the central Rio Grande rift imaged by P and S wave tomography, *J. Geophys. Res.*, *109*, B03305, doi:10.1029/2003JB002743.

Helmberger, D. V. (1973), On the structure of the low velocity zone, *Geophys. J. R. Astron. Soc.*, *34*, 251–263.

Helmberger, D. V., and S. Ni (2005), Approximate 3D body wave synthetics for tomographic models, *Bull. Seismol. Soc. Am.*, *95*, 212–224, doi:10.1785/0120040004.

Helmberger, D. V., and J. E. Vidale (1988), Modeling strong motions produced by earthquakes with two-dimensional numerical codes, *Bull. Seismol. Soc. Am.*, *78*, 109–121.

Komatitsch, D., and J. Tromp (1999), Introduction to the spectral element method for three-dimensional seismic wave propagation, *Bull. Seismol. Soc. Am.*, *139*, 806–822.

Liu, L., and M. Gurnis (2008), Simultaneous inversion of mantle properties and initial conditions using an adjoint of mantle convection, *J. Geophys. Res.*, *113*, B08405, doi:10.1029/2008JB005594.

Liu, L., Y. Tan, D. Sun, M. Chen, and D. Helmberger (2011), Trans-Pacific whole mantle structure, *J. Geophys. Res.*, *116*, B04306, doi:10.1029/2010JB007907.

McCrory, P. A., J. L. Blair, D. H. Oppenheimer, and S. R. Walter (2006), Depth to the Juan de Fuca slab beneath the Cascadia subduction margin: A 3-D model for sorting earthquakes, *Data Ser. 91*, U.S. Geol. Surv., Reston, Va.

Melbourne, T., and D. V. Helmberger (1998), Fine structure of the 410 km discontinuity, *J. Geophys. Res.*, *103*, 10,091–10,102, doi:10.1029/98JB00164.

Melbourne, T., and D. V. Helmberger (2001), Mantle control of plate boundary deformation, *Geophys. Res. Lett.*, *28*, 4003–4006, doi:10.1029/2001GL013167.

Melbourne, T., and D. V. Helmberger (2002), Whole mantle shear structure beneath the East Pacific Rise, *J. Geophys. Res.*, *107*(B9), 2204, doi:10.1029/2001JB000332.

Moschetti, M. P., M. H. Ritzwoller, F.-C. Lin, and Y. Yang (2010), Crustal shear wave velocity structure of the western United States inferred from ambient seismic noise and earthquake data, *J. Geophys. Res.*, *115*, B10306, doi:10.1029/2010JB007448.

Nettles, M., and A. M. Dziewoński (2008), Radially anisotropic shear velocity structure of the upper mantle globally and beneath North America, *J. Geophys. Res.*, *113*, B02303, doi:10.1029/2006JB004819.

Ni, S., V. F. Cormier, and D. V. Helmberger (2003), A comparison of synthetic seismograms for 2D structures: Semianalytical versus numerical, *Bull. Seismol. Soc. Am.*, *93*, 2752–2757, doi:10.1785/0120030011.

Ni, S., D. V. Helmberger, and J. Tromp (2005), Three-dimensional structure of the African superplume from waveform modeling, *Geophys. J. Int.*, *161*, 283–294, doi:10.1111/j.1365-246X.2005.02508.x.

Nikulin, A., V. Levin, and J. Park (2009), Receiver function study of Cascadia megathrust: Evidence for localized serpentinization, *Geochem. Geophys. Geosyst.*, *10*, Q07004, doi:10.1029/2009GC002376.

Obrebski, M., R. M. Allen, F. Pollitz, and S.-H. Hung (2011), Lithosphere-asthenosphere interaction beneath the western United States from the joint inversion of body-wave traveltimes and surface-wave phase velocities, *Geophys. J. Int.*, *185*, 1003–1021, doi:10.1111/j.1365-246X.2011.04990.x.

Pollitz, F. F., and J. A. Snoke (2010), Rayleigh-wave phase-velocity maps and three-dimensional shear velocity structure of the western US from local non-plane surface wave tomography, *Geophys. J. Int.*, *180*, 1153–1169, doi:10.1111/j.1365-246X.2009.04441.x.

Romney, C., B. G. Brooks, R. H. Mansfield, D. S. Carder, J. N. Jordan, and D. W. Gordan (1962), Travel times and amplitudes of principal body phases recorded from GNOME, *Bull. Seismol. Soc. Am.*, *52*, 1057–1074.

Schmandt, B., and E. Humphreys (2010), Complex subduction and small-scale convection revealed by body-wave tomography of the western United States upper mantle, *Earth Planet. Sci. Lett.*, *297*, 435–445, doi:10.1016/j.epsl.2010.06.047.

Sigloch, K., N. McQuarrie, and G. Nolet (2008), Two-stage subduction history under North America inferred from multiple-frequency tomography, *Nat. Geosci.*, *1*, 458–462, doi:10.1038/ngeo231.

Song, T. R. A., and D. V. Helmberger (2006), Low velocity zone atop the transition zone in the western US from S waveform triplication, in *Earth's Deep Water Cycle*, *Geophys. Monogr. Ser.*, vol. 168, edited by S. Jacobson and S. Van der Lee, pp. 195–213, AGU, Washington, D. C.

Song, T. R. A., and D. V. Helmberger (2007a), Validating tomographic model with broad-band waveform modelling: An example from the LA RISTRA transect in the southwestern United States, *Geophys. J. Int.*, *171*, 244–258, doi:10.1111/j.1365-246X.2007.03508.x.

Song, T. R. A., and D. V. Helmberger (2007b), A depleted, destabilized continental lithosphere near the Rio Grande rift, *Earth Planet. Sci. Lett.*, *262*, 175–184, doi:10.1016/j.epsl.2007.07.052.

Sun, D. (2009), Seismic structure of the lower mantle, PhD dissertation, Calif. Inst. of Technol., Pasadena.

Sun, D., and D. V. Helmberger (2011), Upper mantle structures beneath USArray derived from waveform complexity, *Geophys. J. Int.*, *184*, 416–438, doi:10.1111/j.1365-246X.2010.04847.x.

Tape, C., Q. Liu, and J. Tromp (2007), Finite-frequency tomography using adjoint methods—Methodology and examples using membrane surface waves, *Geophys. J. Int.*, *168*, 1105–1129, doi:10.1111/j.1365-246X.2006.03191.x.

Tian, Y., K. Sigloch, and G. Nolet (2009), Multiple-frequency SH-wave tomography of the western United States upper mantle, *Geophys. J. Int.*, *178*, 1384–1402, doi:10.1111/j.1365-246X.2009.04225.x.

Tian, Y., Y. Zhou, K. Sigloch, G. Nolet, and G. Laske (2011), Structure of North American mantle constrained by simultaneous inversion of multiple-frequency *SH, SS*, and Love waves, *J. Geophys. Res.*, *116*, B02307, doi:10.1029/2010JB007704.

VanDecar, J. C., and R. S. Crosson (1990), Determination of teleseismic relative phase arrival times using multi-channel cross-correlation and least squares, *Bull. Seismol. Soc. Am.*, *80*, 150–169.

van der Lee, S., and G. Nolet (1997), Seismic image of the subducted trailing fragments of the Farallon plate, *Nature*, *386*, 266–269, doi:10.1038/386266a0.

van Keken, P. E., B. Keifer, and S. M. Peacock (2002), High-resolution models of subduction zones: Implications for mineral dehydration reactions and transport of water into the deep mantle, *Geochem. Geophys. Geosyst.*, *3*(10), 1056, doi:10.1029/2001GC000256.

Wei, S., Z. Zhan, Y. Luo, S. Ni, Y. Chen, and D. V. Helmberger (2009), Rapid regional centroid solutions, *Eos Trans. AGU*, *90*(52), Fall Meet. Suppl., Abstract S13A-1734.

Xue, M., and R. M. Allen (2007), The fate of the Juan de Fuca plate: Implications for a Yellowstone plume head, *Earth Planet. Sci. Lett.*, *264*, 266–276, doi:10.1016/j.epsl.2007.09.047.

Xue, M., and R. M. Allen (2010), Mantle structure beneath the Western United States and its implications for convection processes, *J. Geophys. Res.*, *115*, B07303, doi:10.1029/2008JB006079.

Zhao, D., A. Hasegawa, and H. Kanamori (1994), Deep structure of Japan subduction zone as derived from local, regional, and teleseismic events, *J. Geophys. Res.*, *99*, 22,313–22,329, doi:10.1029/94JB01149.

R. Chu, D. V. Helmberger, and B. Schmandt, Seismological Laboratory, California Institute of Technology, 1200 E. California Blvd., Pasadena, CA 91125, USA. (chur@gps.caltech.edu)